AGU PUBLICATIONS

Global Biogeochemical Cycles

RESEARCH ARTICLE

10.1002/2014GB004853

Key Points:
- A new method permits us to upscale surface ocean pCO_2 observations
- We find moderate variability in the global ocean carbon sink
- ENSO is the dominant mode driving the sink variability

Correspondence to:
P. Landschützer,
Peter.Landschuetzer@usys.ethz.ch

Citation:
Landschützer, P., N. Gruber, D. C. E. Bakker, and U. Schuster (2014), Recent variability of the global ocean carbon sink, *Global Biogeochem. Cycles*, *28*, doi:10.1002/2014GB004853.

Received 19 MAR 2014
Accepted 6 AUG 2014
Accepted article online 13 AUG 2014

Recent variability of the global ocean carbon sink

P. Landschützer[1,2], N. Gruber[1], D. C. E. Bakker[2], and U. Schuster[3]

[1]Institute of Biogeochemistry and Pollutant Dynamics, ETH Zürich, Zürich, Switzerland, [2]Centre for Ocean and Atmospheric Sciences, School of Environmental Sciences, University of East Anglia, Norwich, UK, [3]College of Life and Environmental Sciences, Hatherly Laboratories, University of Exeter, Exeter, UK

Abstract We present a new observation-based estimate of the global oceanic carbon dioxide (CO_2) sink and its temporal variation on a monthly basis from 1998 through 2011 and at a spatial resolution of 1°×1°. This sink estimate rests upon a neural network-based mapping of global surface ocean observations of the partial pressure of CO_2 (pCO_2) from the Surface Ocean CO_2 Atlas database. The resulting pCO_2 has small biases when evaluated against independent observations in the different ocean basins, but larger randomly distributed differences exist particularly in high latitudes. The seasonal climatology of our neural network-based product agrees overall well with the Takahashi et al. (2009) climatology, although our product produces a stronger seasonal cycle at high latitudes. From our global pCO_2 product, we compute a mean net global ocean (excluding the Arctic Ocean and coastal regions) CO_2 uptake flux of -1.42 ± 0.53 Pg C yr^{-1}, which is in good agreement with ocean inversion-based estimates. Our data indicate a moderate level of interannual variability in the ocean carbon sink (± 0.12 Pg C yr^{-1}, 1σ) from 1998 through 2011, mostly originating from the equatorial Pacific Ocean, and associated with the El Niño–Southern Oscillation. Accounting for steady state riverine and Arctic Ocean carbon fluxes our estimate further implies a mean anthropogenic CO_2 uptake of -1.99 ± 0.59 Pg C yr^{-1} over the analysis period. From this estimate plus the most recent estimates for fossil fuel emissions and atmospheric CO_2 accumulation, we infer a mean global land sink of -2.82 ± 0.85 Pg C yr^{-1} over the 1998 through 2011 period with strong interannual variation.

1. Introduction

The net global uptake of atmospheric carbon dioxide (CO_2) by the ocean plays a major role in reducing its concentration in the atmosphere and moderating the impact of the CO_2 emitted into the atmosphere through anthropogenic activities. Recent estimates [*Mikaloff Fletcher et al.*, 2006; *Wanninkhof et al.*, 2013a; *Le Quéré et al.*, 2014] indicate that roughly one quarter of the anthropogenic CO_2 emitted in the last 20 years was taken up by the ocean, at a mean rate of about 2.0–2.5 Pg C yr^{-1}. The net uptake of CO_2 by the ocean is actually somewhat smaller than the uptake of anthropogenic CO_2, due to the offsetting effect driven by the outgassing of natural CO_2 that stems from carbon that has been added to the ocean by rivers [*Sarmiento and Sundquist*, 1992; *Jacobson et al.*, 2007]. This contemporary global net flux of CO_2 into the ocean has been estimated to be about 1.5 ± 0.5 Pg C yr^{-1} [*Wanninkhof et al.*, 2013a; *Takahashi et al.*, 2009; *Gruber et al.*, 2009].

While there exists a relatively good consensus between different approaches with regard to the estimation of the long-term mean flux [e.g., *Gruber et al.*, 2009; *Wanninkhof et al.*, 2013a], its variability in time and space is much less well known, representing a major source of discrepancies [e.g., *Schuster et al.*, 2013]. This is to a large degree a consequence of the limited observations that make it challenging to verify the time-evolving variations in the ocean carbon sink. This is certainly the case for all those approaches that rely on measurements of the surface ocean pCO_2, i.e., those that employ the bulk parameterization approach and use the partial pressure difference between the atmosphere and the ocean surface layer and an estimate of a gas transfer velocity to estimate the air-sea CO_2 flux [see, e.g., *Wanninkhof et al.*, 2009; *Garbe et al.*, 2014]. To date only one global, interannually varying flux estimate exists that relies largely on this approach [*Rödenbeck et al.*, 2014], although attempts have been made by using the seasonal cycle of surface ocean pCO_2 and projecting its seasonal temperature response to interannual timescales [e.g., *Park et al.*, 2010] and constraining modeled pCO_2 with existing observations [*Valsala and Maksyutov*, 2010; *Majkut et al.*, 2014]. This gap in data and knowledge stands in contrast to that of the annual mean and the seasonal cycle, for which the iconic Takahashi climatology has been regularly updated since its first publication in 1999, i.e., *Takahashi et al.* [1999, 2003, 2009]. The main reason is that although recent pCO_2 databases [*Takahashi et al.*, 2013; *Bakker*

et al., 2014] contain roughly 6 to 10 million observations, the data are still sparse in time and space. Regionally, interannual varying flux estimates exist along regular shipping routes, e.g., in the subtropical Atlantic Ocean along the UK-Caribbean shipping route [*Watson et al.*, 2009]; however, the only place, for which interannually varying flux estimates based on surface ocean pCO_2 data are available for an extended region is the equatorial Pacific, largely thanks to the instrumentation of the Tropical Atmospheric-Ocean project array and the regularity with which these buoys are visited by ships with underway pCO_2 instruments [*Feely et al.*, 1999, 2006].

As a result, most of what is known about the interannual variability of the global ocean carbon sink stems from ocean biogeochemistry models that have been run in hindcast mode, i.e., run over the past few decades with observed atmospheric boundary conditions [e.g., *Le Quéré et al.*, 2000; *McKinley et al.*, 2003; *Wetzel et al.*, 2005; *Le Quéré et al.*, 2007; *Doney et al.*, 2009a; *Le Quéré et al.*, 2010; *Sarmiento et al.*, 2010; *Wanninkhof et al.*, 2013a].

While the different biogeochemical models disagree quite substantially with regard to the exact timing of the interannual variations, they concur that globally, the interannual variability of the sea-air CO_2 fluxes is relatively small and that most of the variability over the last 20 years stems from the equatorial Pacific [*Le Quéré et al.*, 2000; *McKinley et al.*, 2003; *Wetzel et al.*, 2005; *Le Quéré et al.*, 2007; *Doney et al.*, 2009a; *Wanninkhof et al.*, 2013a; *Ishii et al.*, 2014]. The observations from the equatorial Pacific covering by now nearly 30 years support that this region exhibits large fluctuations in the sea-air CO_2 flux. During the positive phase of the El Niño–Southern Oscillation (ENSO) climate mode, i.e., during El Niños, the suppression of upwelling results in less CO_2-rich water near the surface, which in turn leads to a near vanishing of the outgassing of CO_2 that usually characterizes this region. On the other hand, during La Niñas, the unusually strong upwelling of cold, CO_2-rich water leads to an anomalously strong outgassing [*Feely et al.*, 2006]. The first global surface ocean pCO_2 data-based estimate by *Rödenbeck et al.* [2014] supports that the ENSO-driven variability in the tropical Pacific provides the largest contribution to the interannual variability of the global ocean CO_2 flux. Biogeochemical models tend to capture this primarily upwelling-driven interannual variability generally well, resulting in a relatively good agreement between models and observations for the equatorial Pacific [*Le Quéré et al.*, 2000; *McKinley et al.*, 2003; *Peylin et al.*, 2005].

No such agreement exists with regard to interannual variability in the extratropical regions. The few longer-term time series stations from the extratropics suggest a substantial, although not very large amount of interannual variability in the air-sea CO_2 fluxes [e.g., *Gruber et al.*, 2002; *Bates*, 2012]. The available biogeochemical models support the small magnitude, but differ fundamentally with regard to the timing of the variation in the anomalous fluxes [e.g., *McKinley et al.*, 2004; *Schuster et al.*, 2013].

Here we address the long-term mean global ocean carbon sink, its seasonality, and its recent interannual variability from 1998 through 2011 using the two-step neural network approach recently developed by *Landschützer et al.* [2013]. We will show that our globally extrapolated pCO_2 data product compares favorably against independent evaluation data, giving us confidence in the results. Our data will show that the global interannual variability of the air-sea fluxes is relatively modest and mostly governed by the variability in the equatorial Pacific associated with ENSO. Our results will also provide important constraints for the mean land sink and its variability over the 1998 through 2011 period.

2. Data and Methods

The basis for all our analyses are the pCO_2 observations synthesized in the Surface Ocean Carbon Atlas (SOCAT) version 2 (v2) [*Bakker et al.*, 2014] database. We use a two-step neural network approach as described in *Landschützer et al.* [2013] to extrapolate the monthly gridded SOCAT v2 product [*Sabine et al.*, 2013] in space and time and to create monthly sea surface pCO_2 maps at a spatial resolution of $1° \times 1°$ and for the period from 1998 through 2011. From this product, we compute sea-air CO_2 flux maps using a standard bulk formulation and high-resolution wind speeds. We use the mapping approach of *Landschützer et al.* [2013] in an almost identical way compared to its previous application, which considered the Atlantic only. The most important differences are its extension to the globe, excluding the Arctic Ocean, and the use of SOCAT v2 [*Bakker et al.*, 2014] instead of SOCAT version 1.5 [*Pfeil et al.*, 2013], which permits us here to extend the temporal coverage of our neural network estimates through the end of 2011. In the following, we provide a short summary of the method but refer to *Landschützer et al.* [2013] for further details.

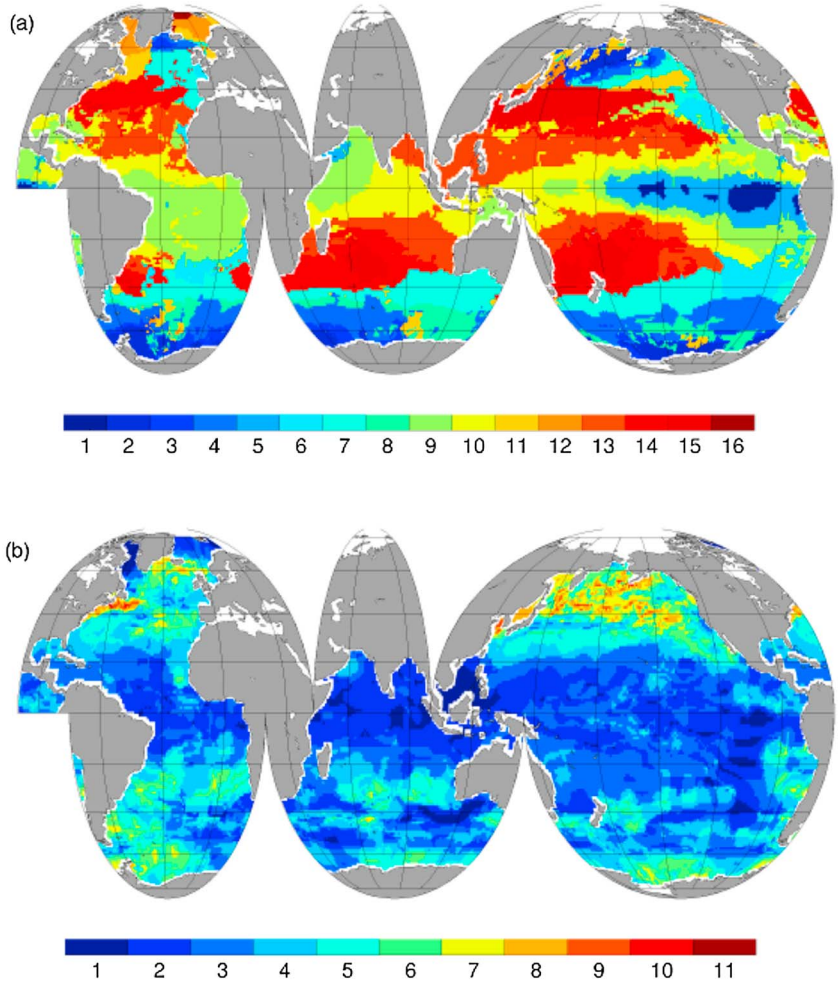

Figure 1. Map of the biogeochemical provinces in the global ocean identified by the Self-Organizing Map (SOM) method: (a) province number of the mode (i.e., most frequent occurrence) and (b) the number of different provinces every pixel belongs to from 1998 through 2011.

The two steps of our mapping approach are as follows: In the first step, the monthly pCO_2 data are clustered into a set of 16 biogeochemical provinces using a Self-Organizing Map (SOM) approach. In the second step, the pCO_2 observations within each biogeochemical province are interpolated using nonlinear functional relationships between a set of input parameters and the observed pCO_2—relationships which were established through a feed-forward neural network (FFN) approach.

For the SOM-based clustering, we used the same four variables as *Landschützer et al.* [2013], namely sea surface temperature (SST) [*Reynolds et al.*, 2002], sea surface salinity (SSS) from Estimating the Circulation and Climate of the Ocean, Phase II (ECCO2) [*Menemenlis et al.*, 2008], mixed layer depth (MLD) from ECCO2 [*Menemenlis et al.*, 2008], and climatological sea surface pCO_2 from *Takahashi et al.* [2009]. As we did not normalize the data, we implicitly weighted the input data toward the seasonal pCO_2 climatology (see discussion in *Landschützer et al.* [2013]). That way, we ensured that we cluster regions together that have a similar seasonal cycle of pCO_2, thereby capturing the most important temporal signal of surface ocean pCO_2 through the temporal evolution of the biogeochemical provinces. This permits us to more accurately reconstruct the remaining variability through the FFN approach. Subsequently, we removed small "island" provinces with a surface area smaller than 10 connected grid cells and replaced them with the province number of the dominant province in the vicinity.

Figure 1 shows the mode of the resulting provinces for each grid cell, i.e., the most frequent occurrence, as well as the number of regions each 1°×1° cell belongs to during the full time period from 1998

Table 1. Statistical Measures of the Comparison of the Global Neural Network-Based Estimates of pCO_2 With the SOCAT v2-Gridded Data [*Bakker et al.*, 2014], Including the Coefficient of Determination (r^2), the Root-Mean-Squared Error (RMSE), the Mean Difference Between SOM-FFN Estimates and SOCAT v2-Gridded Data (Bias), and the Number of Grid Cells

Period	r^2	RMSE (µatm)	Bias (µatm)	# Data
1998–2011	0.88	12.05	−0.12	105,196
1998	0.89	10.85	0.36	5,923
1999	0.87	13.63	−0.07	4,039
2000	0.85	15.79	−0.05	4,827
2001	0.87	15.61	−0.90	4,624
2002	0.88	11.41	−0.12	6,582
2003	0.85	11.53	0.08	6,993
2004	0.88	11.20	−0.18	8,085
2005	0.89	10.91	−0.32	9,243
2006	0.88	11.88	0.10	11,153
2007	0.87	11.99	−0.37	11,111
2008	0.90	11.51	−0.11	9,504
2009	0.84	12.86	0.29	9,650
2010	0.88	9.98	−0.39	9,234
2011	0.88	12.42	−0.11	4,228

through 2011. Regions with strong seasonal pCO_2 variability, such as the higher latitudes, undergo stronger province shifts, resulting in a larger number of provinces per grid cell. However, the vast majority of the grid cells belong to less than five provinces over the entire 168 months of our analysis.

For the FFN-based second step of our method, we divided the SOCAT v2 pCO_2 data of each province into two separate subsets. The first subset is used to train the network, whereas the second subset is used to validate the network output, i.e., to prevent the network from overfitting the heterogeneously distributed data (see *Landschützer et al.* [2013] for more details). Here we use the same SST, SSS, and MLD products as in the SOM step, plus additionally included Globcolour-based chlorophyll *a* (http://www.globcolour.info), the dry air mixing ratio of atmospheric CO_2 (xCO_2) from the GLOBALVIEW marine boundary layer product [*GLOBALVIEW-CO2*, 2011], as well as the deseasonalized components of each input variable as described in *Landschützer et al.* [2013]. Where chlorophyll data were not available due to cloud cover, the pCO_2 fields were estimated by the remaining four proxies and their deseasonalized components.

We calculated our sea-air flux from the difference of the resulting SOM-FFN pCO_2 and the corresponding atmospheric pCO_2 and a gas transfer velocity. For that purpose, atmospheric pCO_2 was estimated from the xCO_2 of the GLOBALVIEW marine boundary layer product [*GLOBALVIEW-CO2*, 2011] and the sea level pressure from the National Centers for Environmental Prediction [*Kalnay et al.*, 1996], taking into account the water vapor correction as described in *Dickson et al.* [2007]. We used high-resolution Cross-Calibrated Multi-Platform (CCMP) wind speeds [*Atlas et al.*, 2011] and the quadratic gas transfer formulation of *Wanninkhof* [1992] rescaled to a global mean gas transfer velocity of 16 cm h^{-1} (to match a recent estimate by *Wanninkhof et al.* [2013a]), to derive the monthly sea-air flux density. In ice-covered regions, the air-sea flux was scaled down to the ice-free part of each grid cell using the monthly sea-ice product of *Rayner et al.* [2003].

Our approach is unique in comparison to other data interpolation algorithms [e.g., *Takahashi et al.*, 2009; *Nakaoka et al.*, 2013; *Rödenbeck et al.*, 2013; *Sasse et al.*, 2013] in that we can produce nearly bias-free estimates on a global scale, while retaining a reasonable amount of fine-scale structure in the observations. In particular, it avoids much of the strong smoothing inherent in the approach used to produce the Takahashi climatologies [e.g., *Takahashi et al.*, 1999]. Compared to previously published SOM-based algorithms [*Telszewski et al.*, 2009; *Nakaoka et al.*, 2013; *Sasse et al.*, 2013], the two-step method has the advantage of producing continuous pCO_2 outputs by reconstructing the nonlinear relationship between driver variables and pCO_2 observations, where data sparse regions benefit from the established relationship within the same preidentified province. Our (nonlinear) regression-based approach provides an alternative CO_2 flux variability estimate compared to the ocean mixed layer process-based method by *Rödenbeck et al.* [2014]. The mixed layer method has the advantage that it permits to link the air-sea CO_2 fluxes explicitly to the underlying processes; however, pCO_2 values for areas without data are interpolated and additionally smoothed.

3. Evaluation and Uncertainties

3.1. Residual Analysis

Globally, the neural network is able to fit the pCO_2 data from SOCAT v2 very well. Table 1 shows the statistical results for the entire time period and individual years, revealing long-term means for the coefficient

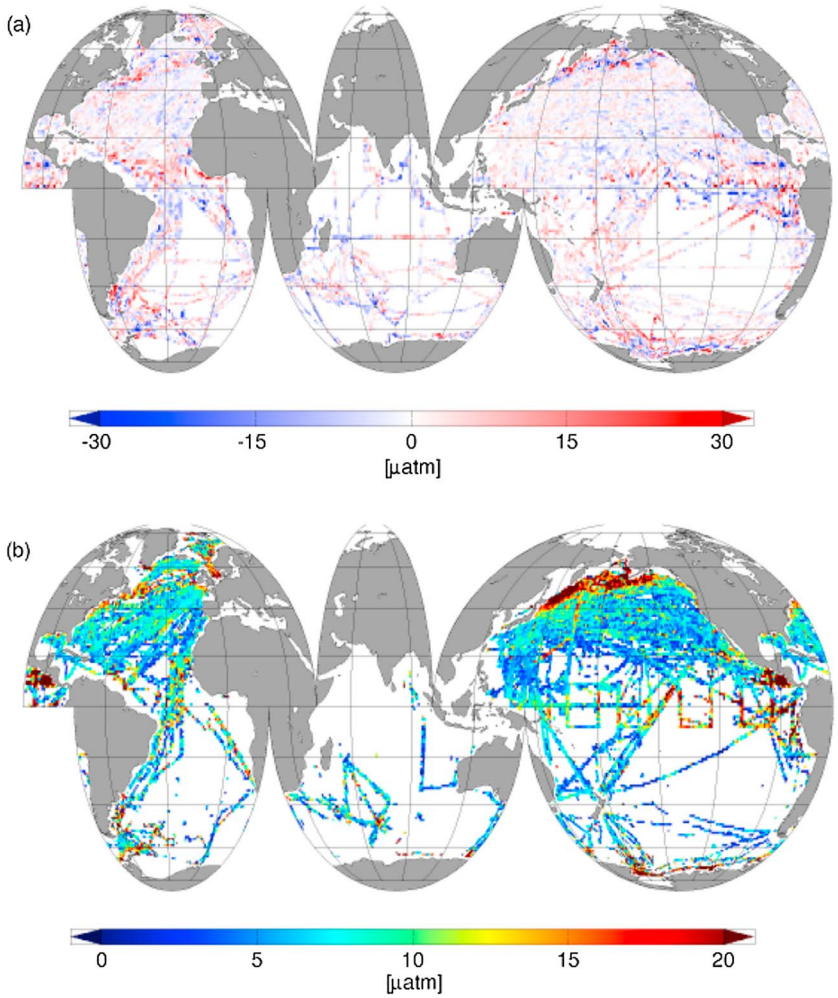

Figure 2. Global maps of (a) temporal mean residuals and (b) standard deviation of the residuals in µatm between neural network estimates and SOCAT v2-gridded observations [*Bakker et al.*, 2014] for the period from 1998 through 2011. Pixels that occur in Figure 2a but are missing in Figure 2b only have one occupation in time.

of determination (r^2) of 0.88, for the root-mean-squared error (RMSE) of 12.05 µatm and a negligibly small overall bias of −0.12 µatm over the entire time period from 1998 to 2011 and for a total of 105,196 gridded observations. This good global fit holds for each individual year with the r^2 ranging from 0.84 to 0.90, the RMSE ranging from 10 µatm to 16 µatm and the annual bias staying within ±1 µatm (Table 1). The RMSE of these global fits are only slightly worse than those we achieved for the Atlantic only [*Landschützer et al.*, 2013], which is reassuring given that we now fit data over a much larger domain. As was the case for the Atlantic basin [see *Landschützer et al.*, 2013], the distribution of the residuals does not depend on the fitted pCO_2 nor on any other of the input variables, confirming that our global estimates are unbiased.

The above conclusions for the global ocean do not apply spatially, as the mean pCO_2 residuals for each grid cell reveal a clear spatial structure, with regions of persistent positive or negative residuals (Figure 2). The largest residuals occur in the high latitudes of both hemispheres, in regions with strong spatial gradients such as on the Patagonian shelf, in the eastern equatorial Pacific and the eastern equatorial Atlantic, and in the Gulf Stream and the North Atlantic Current region. In contrast, other open ocean regions, such as the gyres have comparatively low residuals. The spatial pattern of the mean residuals resembles the spatial patterns of the standard deviation of the residuals (Figure 2b). In fact, the two fields are correlated ($r^2 = 0.49$), suggesting that the relative error of our fits is relatively constant; i.e., that the fits are generally worse in absolute terms when the pCO_2 variability is high in space and time, and better when the variability is small.

Table 2. Validation of the Neural Network Estimates With Data From Time Series Stations[a]

Station	Location	Time Period	RMSE (μatm)	Mean Offset (μatm)
BATS	31.66°N, 64.16°W	1998 through 2011	15.64	0.44
HOT	22.75°N, 158.00°W	1998 through 2011	11.61	0.09
ESTOC	29.04°N, 15.50°W	1998 through 2009	14.50	−7.15
Irminger	64.30°N, 28.00°W	1998 through 2006	22.64	−1.11
CCE1	33.00°N, 122.00°W	2008 through 2010	14.39	−4.11
K2	47.00°N, 160.00°E	2007 through 2009	27.79	−0.16

[a]Stations include the Bermuda Atlantic Time series Station and Hydrostation "S" (BATS) [*Bates*, 2007; *Gruber et al.*, 2002], the Hawaiian Ocean Time series station ALOHA (HOT) [*Dore et al.*, 2009], the European Station for Time series in the Ocean (ESTOC) [*González-Dávila et al.*, 2007], the Irminger Sea station [*Olafsson*, 2007], CCE1 mooring [*Sutton et al.*, 2011], and the K2 time series station [*Wakita et al.*, 2010]. A negative sign for the offset implies that the SOM-FFN estimates are smaller than the validation data.

3.2. Validation With Independent Observations

We validate the SOM-FFN pCO_2 estimates by comparing them to two sets of independent observations that were not included in SOCAT v2 and hence were not used to train the FFN. The first set consists of data from six time series stations (available via http://cdiac.ornl.gov/oceans/Moorings/), while the second set consists of pCO_2 observations that have been included into the LDEOv2012 database [*Takahashi et al.*, 2013] (http://cdiac.ornl.gov/ftp/oceans/LDEO_Database/Version_2012/), but are absent in SOCAT v2.

The data from the six time series stations stem from two very different environments and thus cover a good fraction of the global pCO_2 dynamics. Three of the time series stations are located in the subtropical gyres (the Bermuda Atlantic Time Series and Hydrostation S (BATS) [*Bates*, 2007; *Gruber et al.*, 2002], the Hawaiian Ocean Time series station ALOHA (HOT) [*Dore et al.*, 2009], and the European Station for Time series in the Ocean (ESTOC) [*González-Dávila et al.*, 2007]), while the other three are in temperate to subpolar latitudes (Irminger Sea [*Olafsson*, 2007], CCE1 [*Sutton et al.*, 2011], and K2 [*Wakita et al.*, 2010]) (see Table 2 for details).

The RMSEs between our SOM-FFN estimates and the observations from the different time series stations are similar to those we obtained from the SOCAT v2 data set (see Table 1), i.e., ranging from 11 to 16 μatm. An important exception is the time series stations in the Irminger Sea and in the northwestern North Pacific (K2), where the residuals show a larger spread with a RMSE of 23 to 28 μatm, albeit with a small bias. These stations are in the regions where the standard deviation of the residuals tend to be relatively large (Figure 2b), suggesting that the input parameters at these two stations are not able to fully explain the sea surface pCO_2 variability.

In contrast to the virtually inexistent global bias of our SOM-FFN pCO_2 estimates relative to the training data set, i.e., SOCAT v2 (Table 1), our estimate has a larger mean offset relative to the independent observations from the six time series stations (Table 2). The mean offset for each station ranges from −7 μatm (ESTOC) to 0.5 μatm (BATS). We suspect that potential biases in the calculated pCO_2 from the time series stations contribute to the overall offset, as the computed pCO_2, from the observed DIC and TALK carry uncertainties of up to 6 μatm [see *Millero*, 1995]. Furthermore, a different choice of dissociation constant, e.g., *Peng et al.* [1987], would lead up to a ∼ 9 μatm larger offset at station BATS. But of course, also our SOM-FFN estimates surely contribute to the mean offsets, although we find it reassuring that the mean offset across all six sites is only −2 μatm.

A further test for our SOM-FFN product is how well it is able to represent the temporal evolution of the observed pCO_2 at the six time series sites. As an example, Figure 3 compares the observations from two of the longest running time series stations with the SOM-FFN estimates, i.e., the record from BATS and HOT. While the seasonal cycle is fairly well captured at both stations, month-to-month variabilities are less well reconstructed. It is noteworthy that near Hawaii, the comparison shows a better agreement with the independent HOT data (Figure 3d) than with the colocated data from the SOCAT v2 database, which were actually used for the training.

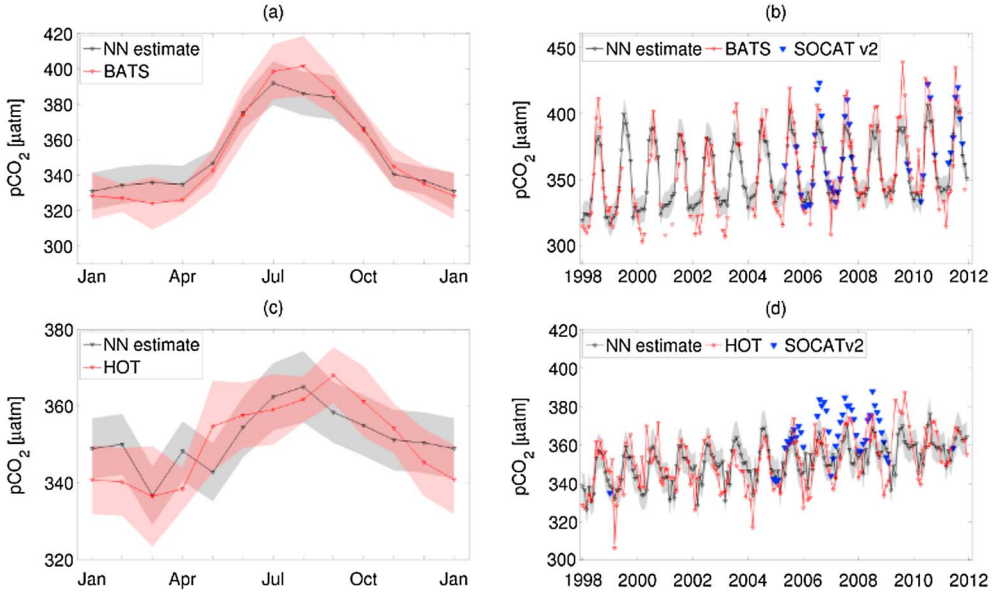

Figure 3. Long-term seasonal cycle and mean seasonal cycle of the neural network estimates compared to (a and b) BATS [*Bates*, 2007; *Gruber et al.*, 2002] and (c and d) HOT [*Dore et al.*, 2009] time series stations. Grey shading shows the uncertainty based on the RMSE of the SOM-FFN estimate. Pink shading shows the standard deviation of the mean seasonal cycle for each time series station. Blue triangles show colocated observations available in SOCAT v2.

In order to evaluate our data across a larger spectrum of the observed pCO_2 dynamics, we turn to the pCO_2 data from the LDEOv2012 database. To identify the extra data that can be used for the evaluation, we first binned all observations of the LDEOv2012 database onto our monthly 1°×1° grid by simply taking the average of all observations within each bin. We then removed all pixels that have data within the gridded SOCATv2 database, leaving only data from stations and cruises that are not included in SOCAT. Overall, from 1998 through 2011, we retrieve 9223 new 1°×1° pixels, corresponding to roughly 10% of the data used in the training (see Table 1). The majority (5424) of the data originate from between 40°S and 40°N, whereas the rest (3799) originate from the high latitudes, i.e., regions where we have identified the strongest neural network-observation discrepancy, as illustrated in Figure 4.

This second test reveals a mean difference across all 9223 evaluation data of 1.48 µatm, confirming our previous conclusion that our estimates are nearly bias free when averaged over larger spatial and temporal domains. The root-mean-squared error of 25.95 µatm is somewhat larger than that we found for all the time series stations together, but actually similar to those from the high-latitude time series stations. If we only consider data within 40°S to 40°N, the bias becomes negligible (−0.25 µatm) and the root-mean-squared error falls to 16.48 µatm.

In summary, the evaluation provides strong evidence that the two-step neural network method is capable of producing essentially bias-free pCO_2 fields once averaged in time and space and that it has no evident tendency for overfitting, i.e., there is no indication that errors relate to the pCO_2 data availability. The accuracy is best in the low latitudes and in the open ocean, but degrades toward the high latitudes.

3.3. Uncertainty of the Air-Sea CO_2 Flux

As the main product of interest is the basin-scale integrated air-sea CO_2 flux, we conduct our uncertainty analysis at this scale, using the 11 ocean regions identified by the Regional Carbon Cycle Assessment and Processes (RECCAP)/Ocean Inversion projects [*Gurney et al.*, 2008; *Mikaloff Fletcher et al.*, 2006] for the spatial integration. As the uncertainty associated with the gas exchange coefficient is of fundamentally different nature, i.e., mostly systematic given it is not well-known functional dependence on wind speed, this source of error is dealt with separately in a second step below. Therefore, we first focus on the uncertainty of the air-sea difference of pCO_2, beginning at the grid level, and then continue at the basin-scale level. For the latter we need to consider the fact that the grid level pCO_2 estimates are highly correlated in space, i.e., that they are not independent.

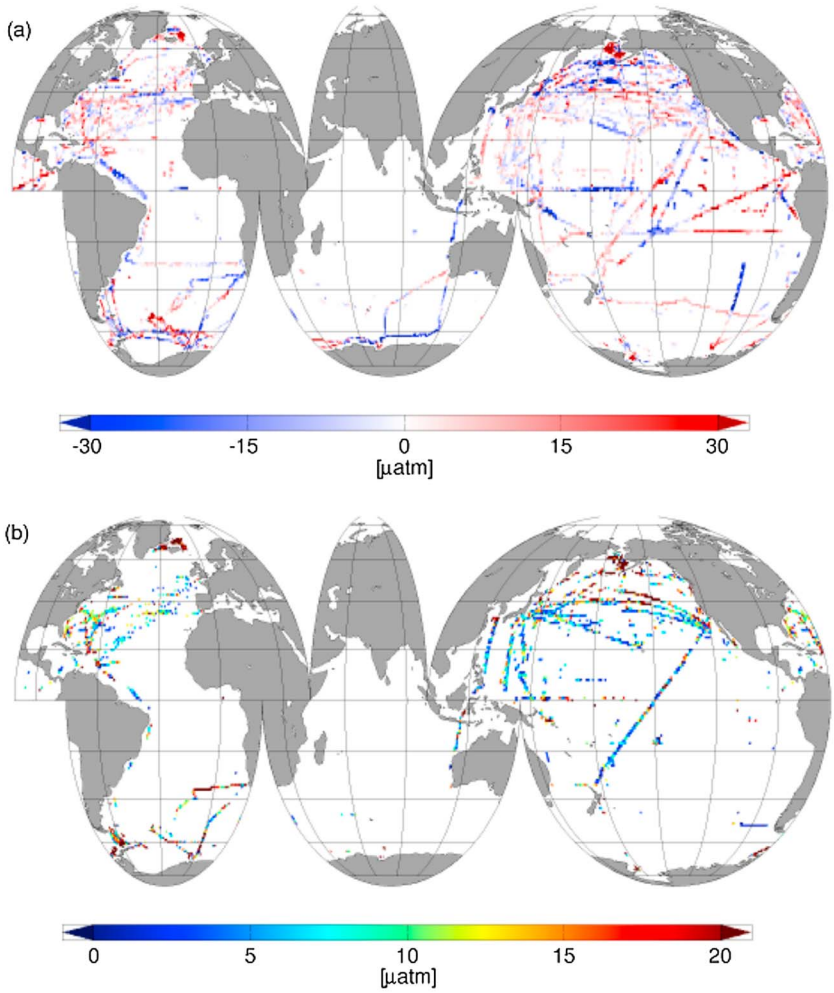

Figure 4. Global maps of (a) temporal mean residuals and (b) standard deviation of the residuals in µatm between neural network estimates and monthly gridded data from the LDEOv2012 database [*Takahashi et al.*, 2013] that are not included in SOCATv2 from 1998 through 2011. Pixels that occur in Figure 4a but are missing in Figure 4b only have one occupation in time.

The uncertainty of the air-sea difference of pCO_2 is dominated by the uncertainty of the oceanic pCO_2, permitting us to neglect the small contribution from the atmospheric pCO_2 (less than 1 µatm). There are three main sources of uncertainty/error for oceanic pCO_2: (i) the measurement error, (ii) the uncertainty stemming from the gridding of the pCO_2 observations into 1°×1° bins, and (iii) the uncertainty introduced by mapping the pCO_2 observations using the SOM-FFN approach. Assuming that these sources of errors are independent, the standard error of the estimated grid level pCO_2, $\sigma(pCO_2)$ can be estimated by the sum of squares [see also *Wang et al.*, 2014].

$$\sigma(pCO_2)^2 = \sigma(\text{meas})^2 + \sigma(\text{grid})^2 + \sigma(\text{map})^2 \quad (1)$$

The measurement error, σ(meas), tends to be the smallest of the three, i.e., about 2–5 µatm [*Pfeil et al.*, 2013; *Wanninkhof et al.*, 2013b], so that we neglect its contribution. For the discretization or gridding error, σ(grid), we adopt a value of 5 µatm based on *Sabine et al.* [2013]. For the mapping error σ(map), we use the mean residuals in each of the 11 oceanic regions, resulting in values ranging from 7 to 17 µatm (with a global average of 12 µatm). With these choices, we arrive at a grid level uncertainty of the mapped pCO_2 product, i.e., $\sigma(pCO_2)$ of between 8.6 and 17.7 µatm, with the majority of the error being determined by the mapping error.

The error of the basin-scale mean oceanic pCO_2, i.e., $\sigma(< pCO_2 >)$ is computed by dividing each error term in (1) by its effective degrees of freedom, N_{eff}, i.e.,

$$\sigma(< pCO_2 >)^2 = \frac{\sigma(\text{grid})^2}{N_{\text{eff}}(\text{grid})} + \frac{\sigma(\text{map})^2}{N_{\text{eff}}(\text{map})} \quad (2)$$

where the chevrons denote the spatial averaging and where we neglected already the contribution of the measurement error.

To estimate the effective degrees of freedom for the gridding error, N_{eff}(grid), we use the global mean decorrelation length scale for oceanic pCO_2 of *Jones et al.* [2012] of 400 km. We calculate the point-to-point distance in kilometers of each pixel within each RECCAP region and calculate N_{eff}(grid) by the effective number of pixels that are outside the decorrelation radius. This is clearly a simplified estimate, as we do not account for temporal and spatial changes of the decorrelation length or the north-south to east-west difference in this number; however, to date, we do not have a sufficiently developed understanding of regional specific length scales.

To estimate the effective degrees of freedom for the mapping error, N_{eff}(map), we determined the spatial decorrelation length of the residuals by analyzing their semivariograms within each region. First, the residuals were divided into a small set of randomly chosen mutually exclusive ensembles with the size of these ensembles being based on the relative data availability. This gave 15 ensembles for the subtropical/temperate North Atlantic, 15 for the subtropical/temperate North Pacific, 10 for the subpolar Atlantic Ocean, 3 for the northern and southern Indian Ocean, and 5 for the remaining regions. We then fitted an exponential function to each semivariogram, resulting in median autocorrelation lengths between 10 km and 957 km for the individual regions. In all cases the semivariograms show a large lag 0 correlation, leading to a relatively low effective number of degrees of freedom.

Adding the error from the data gridding and the SOM-FFN mapping together yields a total mean ΔpCO_2 uncertainty for the 11 RECCAP regions between 2 and 9 μatm. With a global mean gas transfer rate of 0.06 mol C m^{-2} yr^{-1} μatm^{-1}, this results in a flux uncertainty between ±0.02 and ±0.09 Pg C yr^{-1} for the individual regions and a global mean uncertainty of ±0.17 Pg C yr^{-1} calculated by square root of the sum squares propagation.

In the final step, we now include the uncertainty introduced by the gas exchange coefficient. This uncertainty is entirely driven by the uncertainty of the gas transfer velocity, which we estimate by using a measure of the range given by three gas transfer velocity formulations with different wind speed dependencies. These are a quadratic [*Wanninkhof*, 1992], a combination of a quadratic and a cubic [*Nightingale et al.*, 2000] and a cubic relationship [*Wanninkhof and McGillis*, 1999]. The error is then derived from the standard deviation of the resulting flux estimates. We scaled each of these formulations to a global mean gas transfer velocity from 1998 through 2011 of 16 cm h^{-1}, following *Wanninkhof et al.* [2013a], who suggested a mean value of 15.95 h^{-1} on the basis of the CCMP wind product (though for a different time period, i.e., 1990 through 2009). We do this in order to match the strong global constraint provided by the oceanic uptake of bomb radiocarbon [*Sweeney et al.*, 2007; *Naegler*, 2009; *Graven et al.*, 2012a; *Wanninkhof et al.*, 2013a]. In the case of the quadratic relationship, the resulting rescaled transfer resistance factor of 0.254 closely matches the one suggested by *Wanninkhof et al.* [2013a] (0.251). For our analysis we use CCMP winds only, recognizing, however, that the gas transfer velocity is further sensitive to the wind product used.

Combining the uncertainties stemming from ΔpCO_2 and the transfer velocity, using square root of the sum squares propagation, yields an uncertainty of ±0.53 Pg C yr^{-1} for the global long-term mean flux, with the largest fraction of the error stemming from the uncertainty of the gas transfer velocity. The total error corresponds to roughly 37% of the mean global uptake flux reported below. While the air-sea pCO_2 difference error does not change in time, we assume the same uncertainty for each year individually where annual mean results are shown, while uncertainties derived from changes in the gas transfer vary from month to month depending on the wind field.

The error of the interannual variability of the air-sea CO_2 fluxes, i.e., anomalies relative to the long-term mean, is likely smaller than this estimate. This is because a large fraction of the uncertainty is of systematic nature, particularly the part caused by the systematic uncertainty of the gas transfer velocity, and this part falls away when considering year-to-year changes. Allowing for a somewhat larger uncertainty of the

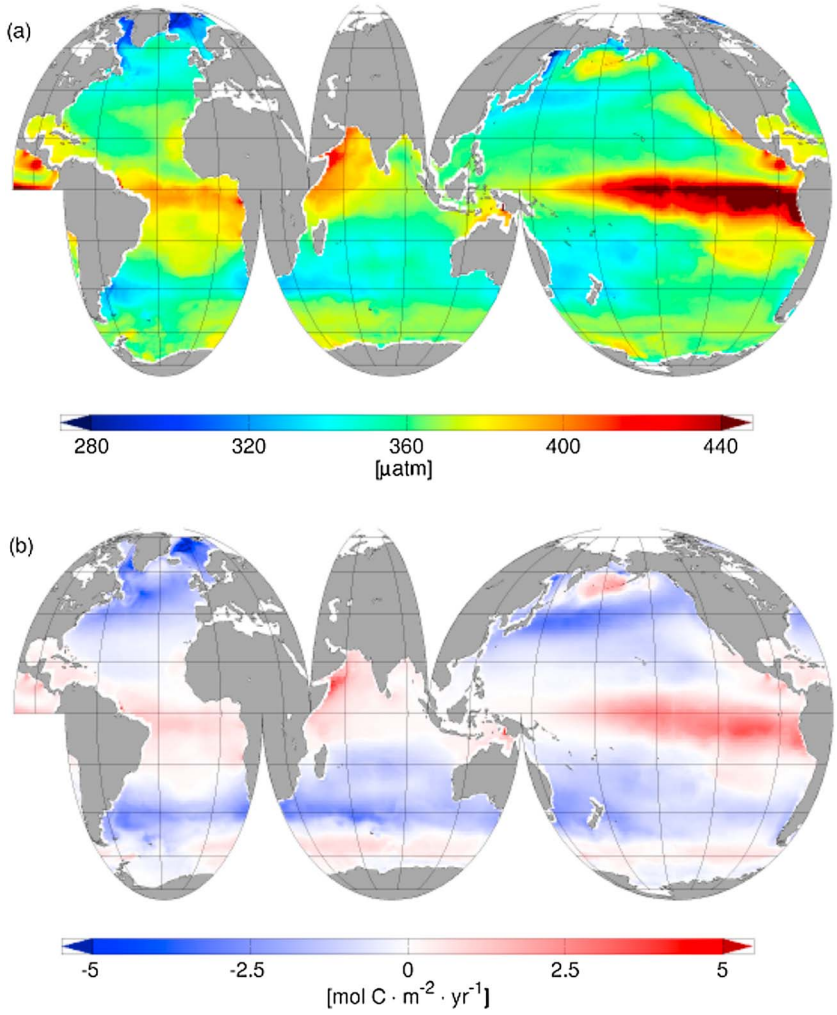

Figure 5. Map of (a) the long-term mean surface ocean pCO_2 and (b) the mean CO_2 flux density in mol C m^{-2} yr^{-1} for the global ocean (excluding the Arctic Ocean) from 1998 through 2011. Negative flux densities indicate CO_2 uptake by the ocean.

ΔpCO_2 on interannual timescales and considering the nonsystematic part of the error associated with the gas transfer velocity, we thus estimate an uncertainty for the interannual anomalies of the global fluxes of about $\pm$0.3 Pg C yr^{-1}.

4. Long-Term Mean pCO_2 and Sea-Air Flux

The highest long-term mean (1998–2011) surface ocean pCO_2 values identified by our SOM-FFN approach occur in the tropical zones of the global ocean, particularly in the eastern equatorial Pacific upwelling area, the northern Indian Ocean, along the Californian Current, and in the high-latitude North Pacific (Figure 5). As these regions are highly supersaturated with regard to atmospheric pCO_2, they act as strong source regions for atmospheric CO_2 (see Figure 5). The lowest sea surface pCO_2 are found in the high-latitude North Atlantic, along the Gulf Stream, along the Kuroshio Current and North Pacific Current, and in the subtropical bands of the Southern Hemisphere. These regions constitute the global ocean's major sink regions for atmospheric CO_2.

The SOM-FFN-based long-term mean pCO_2 pattern largely follow that of the recent Takahashi climatology [*Takahashi et al.*, 2009]. A detailed comparison obtained by averaging our SOM-FFN pCO_2 estimates onto the 4° × 5° grid used by *Takahashi et al.* [2009] and then adjusting them to the same nominal year 2000, by removing 4.5 times the calculated atmospheric pCO_2 trend from our mean SOM-FFN estimate (which is

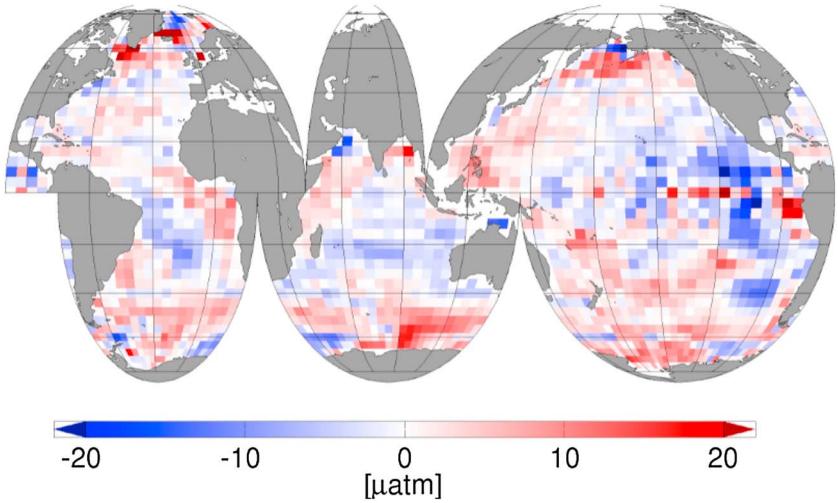

Figure 6. Difference in the surface ocean pCO_2 in µatm between the average neural network estimates (this study), corrected to the year 2000, and the climatology of *Takahashi et al.* [2009]. Positive differences indicate higher pCO_2 for the neural network estimates.

centered between 2004 and 2005), reveals rather small differences for most oceanic regions (Figure 6). The global statistics show that the two fields have an RMSE of 6.13 µatm and a small mean difference of 0.98 µatm. These numbers are similar to those we had obtained for the Atlantic Ocean [*Landschützer et al.*, 2013]. The largest differences occur in the high latitudes of both hemispheres and in the eastern tropical Pacific. The latter is likely linked to the decision of *Takahashi et al.* [2009] to remove observations from El Niño years from their analysis, while the SOM-FFN estimates include observations in these years. Since the surface ocean pCO_2 of the eastern tropical Pacific during El Niño tend to be anomalously low, the Takahashi climatology tends to be biased high as a result, explaining our lower pCO_2. Despite this local discrepancy, the high level of agreement between the two annual mean surface ocean pCO_2 distributions suggests a high robustness of the climatological mean estimates. This is remarkable when considering that the two results were obtained with markedly different mapping methods (a neural network method versus a nonisotropic interpolation method), two very different ways to handle the temporal adjustments (monthly estimates over 14 years combined to form a monthly climatology versus a constant 1.5 µatm/yr adjustment) and two different databases of observations (it should be kept in mind, though, that many of the observations are in both the SOCAT v2 and LDEO databases, although many have undergone distinctly different quality control procedures).

The 14 year-averaged integrated CO_2 flux, derived from the SOM-FFN method, is estimated to be -1.42 ± 0.53 Pg C yr^{-1} (excluding the Arctic Ocean). This is a somewhat larger uptake flux than the most recent estimate based on the Takahashi climatology by *Wanninkhof et al.* [2013a], i.e., -1.18 Pg C yr^{-1} for the reference year 2000, using the same wind product. The two estimates are nearly indistinguishable when the coastal undersampling correction of 0.2 Pg C yr^{-1} by *Wanninkhof et al.* [2013a] is considered, bringing the Takashashi-based uptake estimate to -1.38 Pg C yr^{-1}.

Although the agreement is encouraging, one needs to recollect that these two estimates are strictly speaking not directly comparable. Our global flux is the long-term mean flux for the years 1998 through 2011, while in the case of the Takahashi climatology, the global flux is the flux of a climatological year, referenced to the year 2000.

Both these pCO_2-based estimates refer to the contemporary sea-air flux, as there is no direct way to distinguish between the natural and the anthropogenic component when estimates are derived from surface ocean observations [see *Gruber et al.*, 2009]. However, considering the natural outgassing of riverine carbon of 0.45 ± 0.18 Pg C yr^{-1} [*Jacobson et al.*, 2007] and additionally adding an sea-air flux of -0.12 ± 0.06 Pg C yr^{-1} for the Arctic Ocean [*Schuster et al.*, 2013], we estimate an anthropogenic carbon uptake of -1.99 ± 0.59 Pg C yr^{-1}. This is consistent with the range of recent estimates [e.g., *Gruber et al.*, 2009; *Wanninkhof et al.*, 2013a], but at the lower end of the range. More recently, *Regnier et al.* [2013]

Table 3. Contemporary Mean Sea-Air CO_2 Fluxes for 11 RECCAP/Ocean Inversion Regions and the Major Ocean Basins From (i) This Study (Average From 1998 Through 2011), (ii) Ocean Inversions (Values From Table S1 in *Gruber et al.* [2009]) for the Nominal Period 1995–2000, and (iii) the pCO_2 Climatology of *Takahashi et al.* [2009] for the Reference Year 2000, Using the Same Wind Product and Surface Ocean Area as in (i)[a]

Basin	(i) SOM-FFN This Study (Pg C yr^{-1})	(ii) Ocean Inversion [*Gruber et al.*, 2009] (Pg C yr^{-1})	(iii) pCO_2 Climatology [*Takahashi et al.*, 2009] (Pg C yr^{-1})
Pacific north of 18°N	−0.50 ± 0.11	−0.42 ± 0.08	−0.48
Pacific 18°S–18°N; west of 160°W	0.42 ± 0.09	0.30 ± 0.11	0.43
Pacific 18°S–18°N; east of 160°W	0.04 ± 0.04	0.07 ± 0.04	0.04
Pacific 18°S–44°S	−0.34 ± 0.10	−0.46 ± 0.10	−0.28
Atlantic/Arctic north of 49°N	−0.21 ± 0.06	−0.17 ± 0.07	−0.25
Atlantic 18°N–49°N	−0.21 ± 0.05	−0.32 ± 0.08	−0.20
Atlantic 18°S–18°N	0.10 ± 0.06	0.14 ± 0.06	0.11
Atlantic 18°S–44°S	−0.17 ± 0.03	−0.17 ± 0.05	−0.11
Southern Ocean south of 44°S	−0.21 ± 0.11	−0.34 ± 0.20	−0.32
Indian Ocean north of 18°S	0.09 ± 0.06	0.12 ± 0.06	0.10
Indian Ocean 18°S–44°S	−0.42 ± 0.05	−0.46 ± 0.09	−0.35
Global Ocean	−1.42 ± 0.53	−1.70 ± 0.40	−1.32
Pacific Ocean north of 44°S	−0.38 ± 0.25	−0.51 ± 0.17	−0.29
Atlantic Ocean north of 44°S	−0.50 ± 0.14	−0.52 ± 0.13	−0.45
Southern Ocean south of 44°S	−0.21 ± 0.09	−0.34 ± 0.20	−0.32
Indian Ocean north of 44°S	−0.32 ± 0.08	−0.34 ± 0.11	−0.25

[a]Basin-wide uncertainties for the SOM-FFN and the Ocean Inversion were calculated using standard error propagation of the individual uncertainty estimates derived for the 11 RECCAP/Ocean Inversion regions.

suggested that the river outgassing flux may have increased relative to preindustrial conditions as a result of anthropogenic activities. This would require a larger river outgassing adjustment (by 0.1 Pg C yr^{-1} or more), increasing the implied anthropogenic carbon uptake by the same amount.

Table 3 compares the long-term mean results of this study to the results obtained by the Ocean Inversion study of *Gruber et al.* [2009] and the climatology product of *Takahashi et al.* [2009] for each of the 11 RECCAP/Ocean Inversion regions. Overall, there is strong agreement between the different estimates with regard to the magnitude and the direction of the flux. In general, the strongest differences occur in ocean areas where the least observational coverage exists, i.e., the South Pacific, the Southern Ocean, and the Southern Indian Ocean.

The Ocean Inversion estimates show the strongest sink per basin. Strong CO_2 uptake in the North Pacific Ocean is almost balanced by the strong outgassing in the tropical Pacific. There is particular good agreement regarding the Atlantic Ocean uptake within all methods, which constitutes the strongest sink of all basins. The SOM-FFN basin fluxes are often located in-between the *Takahashi et al.* [2009] product and the Ocean Inversion product. The largest difference between the SOM-FFN and the other estimates is found in the Southern Ocean, where the integrated uptake flux is ~ 0.1 Pg C yr^{-1} smaller. This may reflect differences in the methods, but also could be real, owing to the potentially substantial trends in the air-sea CO_2 fluxes in this region [*Le Quéré et al.*, 2007; *Lovenduski and Gruber*, 2008; *Lenton et al.*, 2013] and the different periods covered by the three data products.

5. Seasonality

The 14 year mean seasonal cycle of the air-sea CO_2 flux density reveals a clear pattern across the different ocean basins (Figure 7). These seasonal variations in the CO_2 flux densities are largely driven by the strong seasonal cycles of the surface ocean pCO_2, and only modified by the seasonal cycles in atmospheric pCO_2 and in the gas transfer velocity. We therefore discuss only the fluxes. The broadscale pattern of the fluxes is similar in the different basins, but there also exist substantial differences.

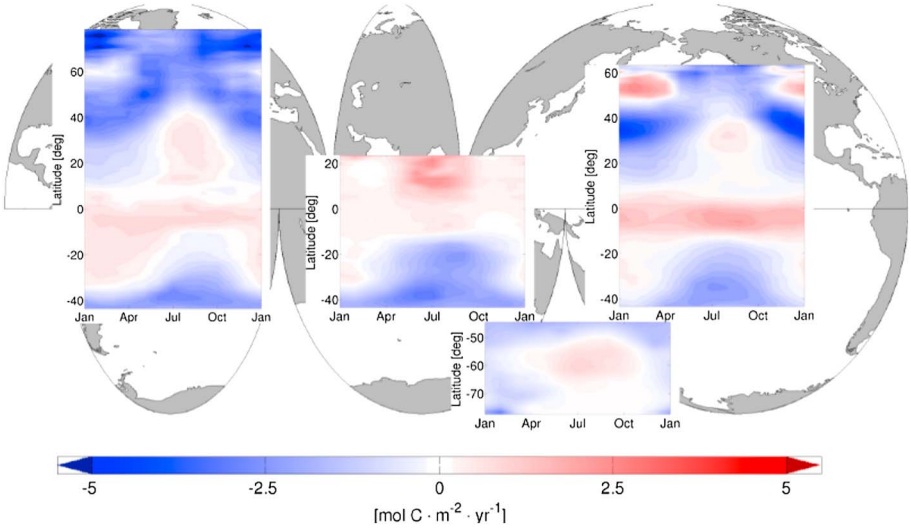

Figure 7. Hovmoeller plots of the mean seasonal cycle from 1998 through 2011 of the zonally averaged air-sea flux density (mol C m^{-2} yr^{-1}) for the four major ocean basins, namely the Pacific Ocean, the Atlantic Ocean, the Southern Ocean, and the Indian Ocean. Negative or blue values indicate uptake of CO_2 by the ocean.

The seasonal cycle of the zonally averaged CO_2 flux density of the Pacific Ocean north of 44°S shows that the equatorial Pacific is a strong outgassing region throughout the entire year, linked to the upwelling of carbon-rich waters from deeper layers. There is a distinct seasonal cycle in the lower latitudes (equatorward of 40°N and 40°S) of both hemispheres resulting in wintertime uptake of CO_2 by the ocean and summertime outgassing. The seasonal cycle in the high-latitude North Pacific (north of 40°N) is antiphased compared to that in the subtropical cycle. This is the result of a poleward transition from a temperature-controlled seasonal cycle with a pCO_2 maximum in summer to one that is controlled by biological drawdown in summer and physical resupply of CO_2 from deeper layers in winter, giving rise to a pCO_2 maximum in winter [*Takahashi et al.*, 2002; *Sarmiento and Gruber*, 2006].

The mean seasonal cycle of the flux density in the Atlantic Ocean (44°S–79°N and west of 30°E) is largely unchanged from that reported by *Landschützer et al.* [2013] despite the addition of data from 2008 through 2011 (Figure 7). The seasonal cycle is also very similar to that of the Pacific Ocean, as both basins are stretching along similar latitudes. However, there are significant differences. The equatorial band of the Atlantic Ocean shows lower flux densities throughout the entire year than that of the Pacific Ocean. Furthermore, the band from 40°N to 60°N has a much larger seasonal amplitude in the Pacific Ocean than in the Atlantic Ocean.

The CO_2 flux density in the Southern Ocean (south of 44°S) follows a clear seasonal pattern, with CO_2 uptake in the Southern Hemisphere summer (December to March). In contrast, there is outgassing of CO_2 from 50°S to 65°S in the Southern Hemisphere winter (July to October). Only a small band in the northern part of this basin (from 44°S to 50°S) remains an uptake region all year round.

The seasonal cycle of the Indian Ocean (north of 44°S) flux density (Figure 7) reveals a distinct equatorial CO_2 source from 10°N to 10°S throughout the entire year. Further to the north, the neural network estimates identify a high CO_2 outgassing region from October to May with an additional monsoon-driven [see, e.g., *Sarma et al.*, 2013] flux increase from May to October. South of the equator the Indian Ocean has a similar seasonal flux pattern compared to that in the South Atlantic and the South Pacific.

In contrast to the long-term mean, there is less agreement between our SOM-FFN-based flux estimates and those of *Takahashi et al.* [2009] with regard to the seasonality of the sea surface pCO_2. Figure 8 reveals that in particular in the high-latitude North Pacific, North Atlantic, and the northern Indian Ocean, zonally averaged differences exceed ±20 µatm leading to substantially larger seasonal amplitudes in these areas in our estimates. Given the high level of temporal and spatial smoothing applied by *Takahashi et al.* [2009] to map their data, their lower level of seasonal variations is not unexpected; however, it has to be noted here that

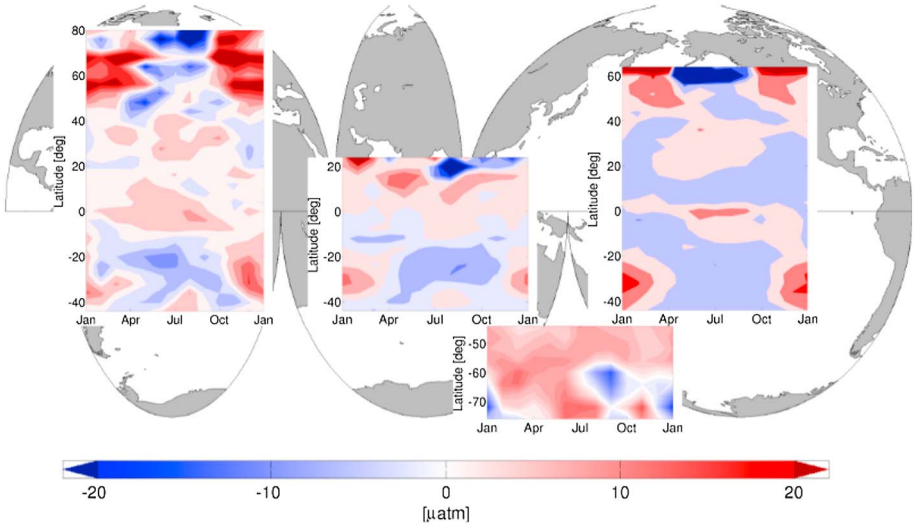

Figure 8. Zonally averaged difference between the SOM-FFN and the *Takahashi et al.* [2009] pCO_2 seasonal cycle for the four major ocean basins, namely the Pacific Ocean, the Atlantic Ocean, the Southern Ocean, and the Indian Ocean. The SOM-FFN seasonal cycle was corrected to the reference year 2000, as explained in the text, to be comparable to the *Takahashi et al.* [2009] climatology.

the SOM-FFN also has the largest residuals in these areas. In contrast, within the low latitudes, differences are well within 10 µatm.

6. Interannual Variability

Our SOM-FFN-based global contemporary air-sea flux exhibits a modest level of year-to-year variability from 1998 through 2011 with a minimum carbon uptake of -0.80 ± 0.52 Pg C yr^{-1} in 2001 and a maximum uptake of -2.01 ± 0.59 Pg C yr^{-1} in 2011 and with a standard deviation of the deseasonalized and detrended (to separate the effect of short-term trends) monthly fluxes of (± 0.12 Pg C yr^{-1}). This confirms the results of many previous studies that the amount of interannual variability of the ocean sink is small [*Battle et al.*, 2000; *Le Quéré et al.*, 2000, 2003; *Wanninkhof et al.*, 2013a], but substantial differences in the annual mean flux arise from trend signals. The most recent estimate by *Rödenbeck et al.* [2014] of ± 0.31 Pg C yr^{-1} suggests a twice as large value; however, this latter estimate is for the 1993–2008 period, which includes the largest El Niño event of the past decades, i.e., the 1997/1998 event.

Nearly all of the interannual variability of the air-sea CO_2 fluxes is driven by changes in the surface ocean pCO_2, and little by changes in the gas transfer velocity. We tested this by keeping the ΔpCO_2 constant for the entire time period, applying the 14 year monthly average ΔpCO_2 values for each year individually. The resulting annual mean gas fluxes range from -1.35 Pg C yr^{-1} to -1.50 Pg C yr^{-1}, i.e., the peak-to-peak variability is only $\sim$ 13% from the observed peak-to-peak variability with variable ΔpCO_2. We thus focus our further discussion on the oceanic pCO_2-induced variability only.

In order to investigate the regions driving the global pCO_2 variability, we deseasonalized our pCO_2 fields using a 12 month running average filter and detrended them by removing the linear trend for each grid cell from 1998 through 2011. The map of the standard deviation of the resulting interannual sea surface pCO_2 anomalies (Figure 9a) reveals the strongest variability within the equatorial Pacific and the high-latitude Atlantic and Pacific Ocean, confirming previous model-based [e.g., *McKinley et al.*, 2004] and observation-based [*Rödenbeck et al.*, 2014] findings that have identified these regions as hot spots of interannual variability.

An empirical orthogonal function (EOF) analysis of the interannual anomalies of pCO_2 illustrates that most of this variability in the western equatorial Pacific is of a coherent nature, i.e., is organized to form the globally leading EOF mode (Figure 9b) explaining 28% of the global variability in surface ocean pCO_2. Due to the size of the pCO_2 covariance matrix needed to compute the EOFs, we had to coarsen the SOM-FFN pCO_2 estimates from their original $1° \times 1°$ resolution to $2° \times 2°$. Tests over smaller domains revealed that this coarsening had no impact on the results. The time series of this leading global EOF, i.e., its principal component,

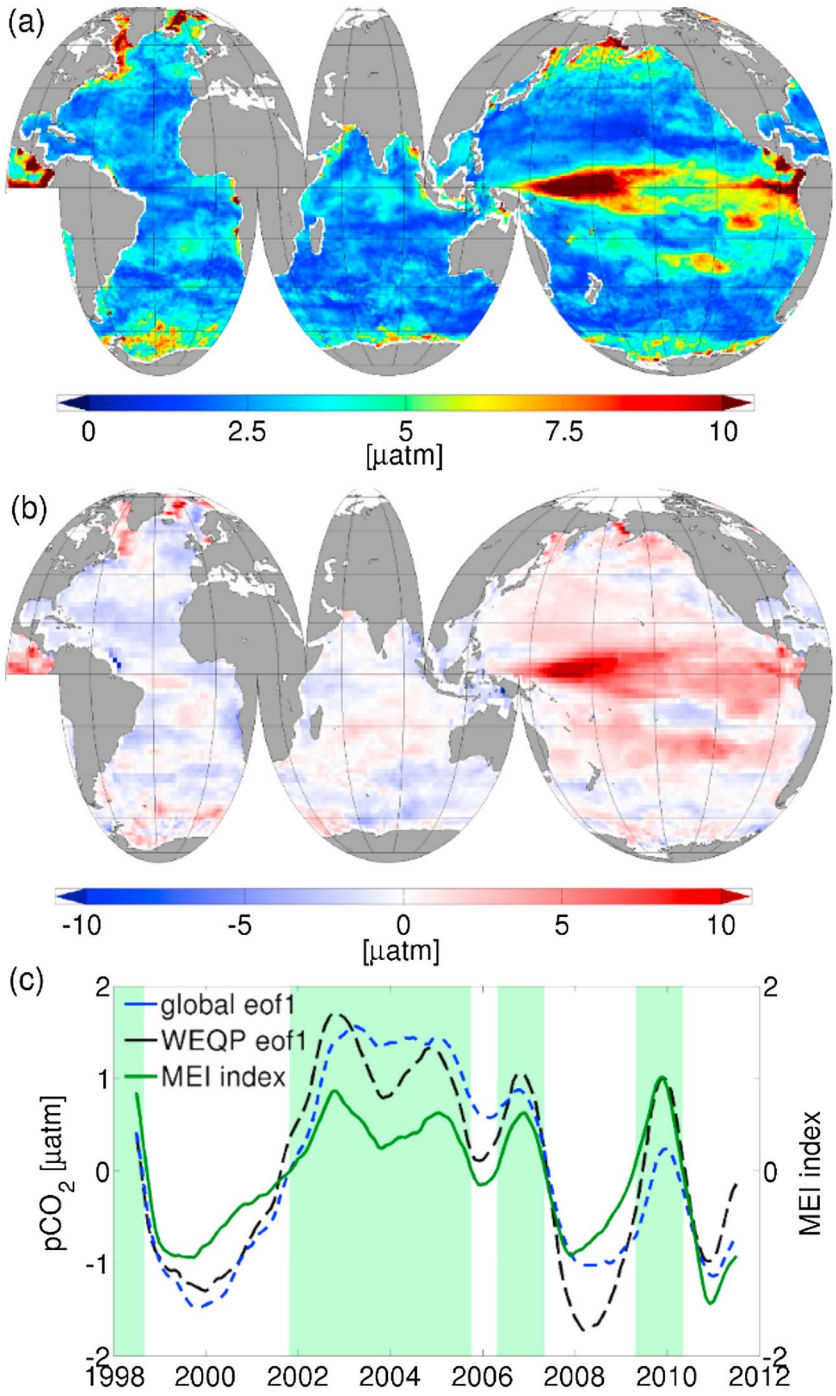

Figure 9. Variability of the sea surface pCO_2 illustrated as (a) the 1998 through 2011 standard deviations of the interannual anomalies of surface ocean pCO_2 fields (obtained by deseasonalizing and detrending the data), (b) the spatial distribution of the amplitude of the first (leading) empirical orthogonal function (EOF) of the interannual anomalies of pCO_2 (data are rescaled to 2° longitude × 2° latitude), and (c) the time series of the leading EOF's of the western equatorial Pacific (WEQP, 15°S to 15°N and west of 160°W) and the global ocean compared to the Multivariate ENSO Index [*Wolter and Timlin*, 2011]. The green areas highlight positive Multivariate ENSO Index (MEI) phases.

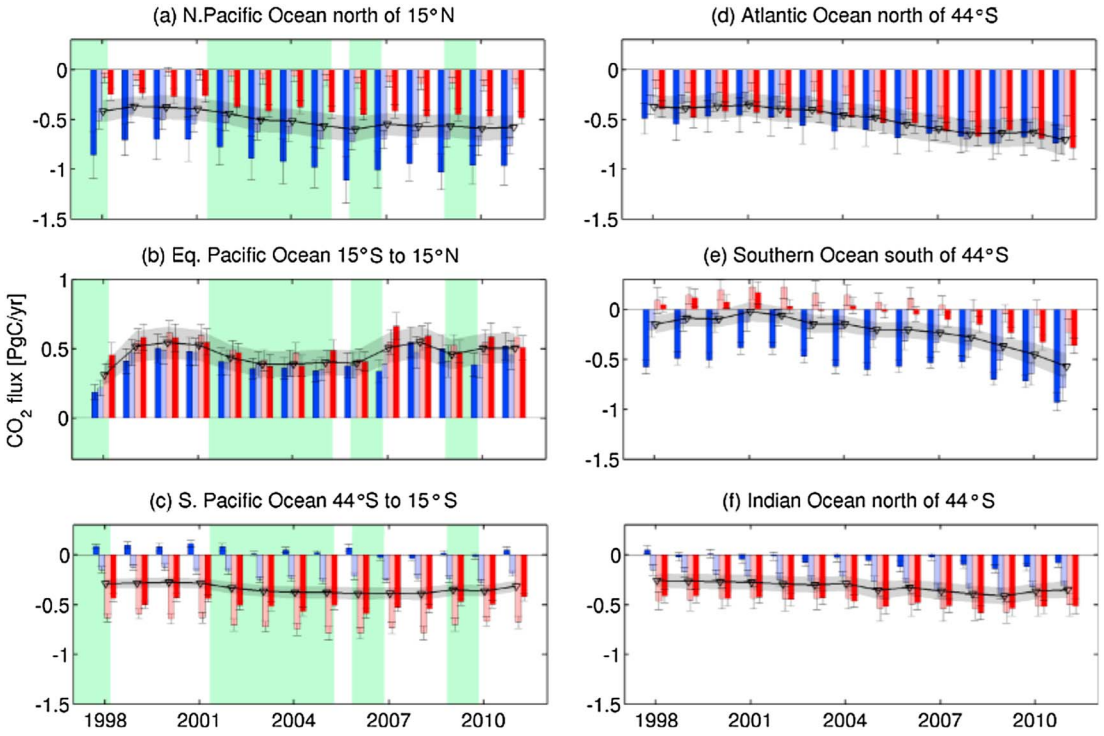

Figure 10. Seasonal and annual mean fluxes from 1998 to 2011 for the four major ocean basins, (a–c) the Pacific Ocean (green areas highlight positive MEI phases), (d) the Atlantic Ocean, (e) the Southern Ocean, and (f) the Indian Ocean. Dark blue shows the results for the Northern Hemisphere winter months (December-January-February), light blue the spring months (March-April-May), light red the summer months (June-July-August), and dark red the autumn months (September-October-November). The annual mean flux is plotted as a black line on top. Error bars indicate the uncertainty range of the air-sea flux estimate in section 3.3.

is highly correlated ($r = 0.85$) with the Multivariate ENSO Index (MEI, http://www.esrl.noaa.gov/psd/enso/mei/ [*Wolter and Timlin*, 2011]), confirming the dominant role of ENSO for controlling interannual variability in global air-sea CO_2 fluxes. The dominance is even larger when we perform an exclusive EOF for the western equatorial Pacific area (15°S to 15°N and west of 160°W), where the leading EOF explains 72% of the variance. In contrast to the first global EOF mode, the second and third EOF modes (15% and 10%) reveal relatively little large-scale spatial coherence and are therefore neither shown nor discussed here. Next, we discuss the interannual variations in each basin in turn.

6.1. Pacific Ocean

With an interannual variability of the air-sea CO_2 flux of ± 0.11 Pg C yr^{-1} ($\pm$ 1 standard deviation), the Pacific Ocean north of 44°S dominates the global ocean flux variability. From 1998 through 2011 the Pacific flux varied from an uptake minimum of -0.11 ± 0.25 Pg C yr^{-1} in the year 2000 to an uptake maximum of -0.59 ± 0.23 Pg C yr^{-1} in 2006. As suggested already by the EOF analysis, Figures 10a–10c show that most of this variability stems from the equatorial region, with the strong reduction in the whole Pacific sink strength in the early 2000s having been caused by the stronger than usual outgassing in the equatorial subregion owing to the strong La Niña that occurred there after the 1997/1998 El Niño (Figure 10b). But also the more moderate fluctuations in the equatorial Pacific after 2000 largely reflect the impact of ENSO, with years having positive anomalies of the MEI characterized by weaker outgassing and vice versa for negative anomalies. These ENSO-induced fluctuations are in excellent agreement with the findings of *Feely et al.* [2006], who analyzed ENSO-induced variations in the equatorial Pacific over a more extended period.

The ENSO cycles in the last 20 years tended to have their maximum anomalies in sea surface temperature in the central equatorial Pacific and to a lesser degree in the eastern equatorial Pacific as was the norm before *Fedorov and Philander* [2000], a pattern often referred to as El Niño Modoki [e.g., *Ashok et al.*, 2007]. The spatial pattern of the interannual standard deviation and of the leading EOF (Figure 9) clearly reflect this central Pacific ENSO pattern as well. It is thus instructive to split this area at 175°W in order to separately analyze the variability in the western Pacific warm pool and the eastern equatorial upwelling area. Furthermore, it

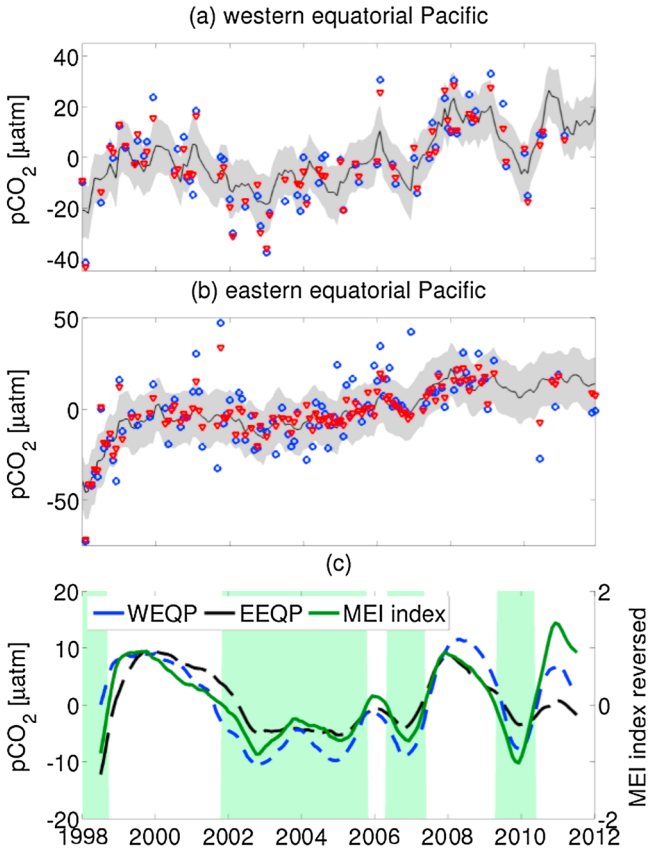

Figure 11. Temporal evolution of the interannual pCO_2 anomalies (a) in the western equatorial Pacific (10°S to 10°N; 165°E to 175°W) and (b) in the central and eastern equatorial Pacific (10°S to 10°N; 175°W to 90°W). The black line shows the spatial average pCO_2 within each box and the associated spatial standard deviation is marked with a grey shade. Blue circles depict the average observed sea surface pCO_2 anomaly within each box (calculated from the SOCAT v2-gridded data) and the red triangles show the average neural network pCO_2 colocated to these measurements. (c) The interannual pCO_2 anomaly of each of the western equatorial Pacific (WEQP) and the eastern equatorial Pacific (EEQP) (left axis in µatm = detrended and smoothed using a 12 month running average filter) is compared to the MEI index (right axis = smoothed using a 12 month running average filter as well and reversed for better comparison). The green areas highlight positive MEI phases.

behooves us to demonstrate how well the SOM-FFN-based estimates are able to capture the observed pCO_2 variability through time in these two subregions.

Figures 11a and 11b illustrate the large interannual pCO_2 anomalies in each of these two boxes, but also how well the colocated SOM-FFN-based pCO_2 anomalies are able to capture the observed anomalies, especially their interannual fluctuations. The interannual pCO_2 anomalies of the observations were computed by subtracting the SOM-FFN long-term climatological value for that month and grid cell. The high temporal density of the observations and the good fit permit us to have relatively high confidence in the SOM-FFN-based estimates of the interannual pCO_2 variability in the equatorial Pacific.

There is, however, also a tendency for the SOM-FFN-based estimates to underestimate the observed variations, but this occurs primarily on monthly to seasonal timescales, where tropical instability waves [*Feely et al.*, 1994], individual Kelvin waves, and other physical perturbations alter surface ocean pCO_2 in a manner that our approach is not able to capture. When the differences between the SOM-FFN and the observed anomalies are computed over the full annual cycle by removing the SOM-FFN 14 year mean seasonal cycle, no temporal structure in the bias emerges, thus giving us good confidence in our estimates capturing the interannual variations.

The spatially averaged interannual pCO_2 variations in both the eastern and western equatorial Pacific box have a very high correlation with the multivariate ENSO index (r = 0.74 and r= 0.89) (Figure 11c), confirming our EOF-based analyses above, which suggested that 72% of the variance in the equatorial Pacific is linked to ENSO. The even somewhat higher correlation in the western equatorial Pacific reflect also the more Modoki-style ENSO dominance over the last 20 years.

The year-to-year flux variability in the extratropical Pacific is much smaller than that in the equatorial band (Figure 10), but within the 14 year period still substantial, especially in the North Pacific, where the minimum minus maximum annual fluxes differ by ~0.3 Pg C yr^{-1}. This variability pattern is weakly correlated to the Pacific Decadal Oscillation index [*Mantua et al.*, 1997].

6.2. Atlantic Ocean

The variability and trends of the Atlantic Ocean north of 44°S have been discussed by *Landschützer et al.* [2013] for the time period 1998 through 2007, so we focus here only on those aspects that emerge by the extension of the time period to December 2011. Small additional changes emerge in the years before 2007

due to the addition of new data in the SOCAT v2 data set, in particular for the years 2005 to 2007 [*Bakker et al.*, 2014]. Figure 10d shows a close to steady carbon flux from 1998 through 2003, followed by a trend toward an increasing carbon sink until 2011, when the uptake peaks with a flux of -0.71 ± 0.16 Pg C yr^{-1}. Thus, the trend toward a stronger Atlantic sink identified by *Landschützer et al.* [2013] is found to persist through 2011 and even starts 1 year earlier than originally diagnosed. The standard deviation of the interannual variability of ± 0.03 Pg C yr^{-1} is low across the basin and also within each hemisphere, in line with the prior results [*Landschützer et al.*, 2013].

On average, the uptake fluxes of the North Atlantic exceed the uptake fluxes of the South Atlantic (see Table 3). Both basins, however, undergo similar year-to-year changes with both basins having had the weakest sink in 2001 (-0.33 ± 0.12 Pg C yr^{-1} in the Northern Hemisphere and -0.03 ± 0.11 Pg C yr^{-1} in the Southern Hemisphere) and the strongest sink in 2011 (-0.51 ± 0.15 Pg C yr^{-1} in the Northern Hemisphere and -0.19 ± 0.13 Pg C yr^{-1} in the Southern Hemisphere), leading to a peak-to-peak flux difference of almost 0.2 Pg C yr^{-1} in both hemispheres.

6.3. Southern Ocean

The Southern Ocean, defined here as the ocean south of 44°S, is the largest of the four basins and remains strongly undersampled with respect to its large surface area (see Figure 2). Thus, it remains the basin with the weakest observational constraints and thus in relative terms the ocean area with the largest uncertainties.

The annual mean SOM-FFN pCO_2-based flux estimates for the Southern Ocean have the largest range of all basins, varying between an absolute minimum of -0.02 ± 0.10 Pg C yr^{-1} in 2001 and an absolute maximum of -0.57 ± 0.13 Pg C yr^{-1} in 2011 (Figure 10e). Despite this considerable range, the standard deviation of the interannual variability of ± 0.06 Pg C yr^{-1} is relatively modest, largely owing to the gradual nature of the flux variations.

The Southern Ocean carbon sink weakened from 1998 to 2001, but then the trend reversed sign and the sink strengthened substantially until 2011 (Figure 10e). A possible explanation for this recent reinvigoration of the Southern Ocean carbon sink after a long-term weakening trend [*Le Quéré et al.*, 2007] is the change in the Southern Annular Mode, as it recently tended to become neutral or even negative following the 1998 maximum [*Marshall*, 2003]. A high-index polarity of the Southern Annular Mode (SAM) leads to an increase of the westerly winds resulting in stronger upwelling, which increases the surface ocean pCO_2 and hence the outgassing of CO_2 [*Lovenduski et al.*, 2007; *Lenton and Matear*, 2007]. The recent trend toward a lower SAM index thus creates the opposite tendency, i.e., an increase in the uptake of CO_2, as suggested by *Fay and McKinley* [2013].

Overall, our Southern Ocean mean flux compares fairly well with the *Takahashi et al.* [2009] observation-based estimate from *Lenton et al.* [2013] and slightly worse to the recalculated *Takahashi et al.* [2009] based flux estimate in Table 3 of this study (-0.21 ± 0.11 Pg C yr^{-1} in this study compared to -0.27 ± 0.13 Pg C yr^{-1} in *Lenton et al.* [2013] and -0.32 in Table 3).

6.4. Indian Ocean

Compared to the other ocean basins, the Indian Ocean shows the lowest year-to-year variability (Figure 10f), with a maximum CO_2 uptake in 2009 of -0.41 ± 0.09 Pg C yr^{-1} and a minimum uptake in 1998 of -0.25 ± 0.07 Pg C yr^{-1}. This basin further shows the weakest increase in the carbon sink compared to the other basins from 1998 through 2011. The interannual variability is estimated to be ± 0.02 Pg C yr^{-1} and is substantially smaller than, e.g., in the Pacific Ocean.

6.5. The Global Ocean

In order to better compare our SOM-FFN-based estimates of the contemporary air-sea CO_2 flux with model-based results as well as other estimates, we need to include a flux value for the Arctic and need to make a correction for the outgassing of riverine carbon. We use the same values as above (Arctic uptake flux of -0.12 Pg C yr^{-1} [*Schuster et al.*, 2013] and river outgassing of 0.45 Pg C yr^{-1} [*Jacobson et al.*, 2007]), but further assume that these fluxes are not changing over the 1998 through 2011 period. The long-term mean of this adjusted flux corresponds essentially to the oceanic uptake of anthropogenic CO_2 (see above), but the interannual variations are likely driven by natural CO_2 uptake.

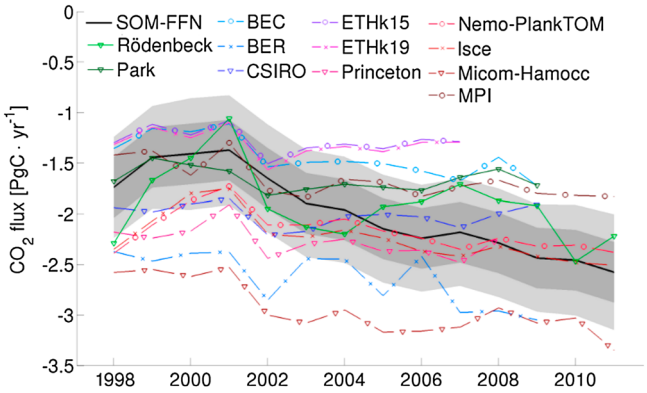

Figure 12. Comparison of the annual integrated anthropogenic CO_2 flux based on the SOM-FFN approach (black line) with model and observation-based results included in the Global Carbon Budget and the RECCAP ocean studies (references in the text). Light shading illustrates the uncertainty interval of the SOM-FFN estimate for each year and dark shading illustrates the estimated anomaly uncertainty (see section 3.3).

The evolution of the thus adjusted global uptake of CO_2 is illustrated in Figure 12 in comparison to recent observation and model-based estimates [*Rödenbeck et al.*, 2014; *Park et al.*, 2010; *Galbraith et al.*, 2010; *Ilyina et al.*, 2013; *Assmann et al.*, 2010; *Doney et al.*, 2009b; *Aumont and Bopp*, 2006; *Buitenhuis et al.*, 2010; *Matear and Lenton*, 2008; *Graven et al.*, 2012b] included in the Global Carbon Project (www.globalcarbonproject.org) and additional model-based estimates from the RECCAP project ocean studies. Our SOM-FFN-based global CO_2 uptake estimate exhibits modest year-to-year variability within the period from 1998 through 2011 with a minimum carbon uptake of -1.37 ± 0.57 Pg C yr^{-1} in 2001 and a maximum uptake of -2.58 ± 0.60 Pg C yr^{-1} in 2011 (see Figure 12). The SOM-FFN estimate is on the lower end of all estimates in the first year of the analysis period, but shows a substantially stronger sink trend from 2001 onward.

The linear trend evolving within this 14 year time period (linear fit to the estimates, smoothed using a 12 month running mean filter) is estimated to be -1.00 ± 0.12 Pg C yr^{-1} decade^{-1}. The uncertainty of the trend is estimated as the standard deviation of the trend residuals (the smoothed estimates minus the SOM-FFN estimates along the fitted linear trend line). When only the start and end year annual mean CO_2 flux is taken into account, the trend reduces to -0.60 Pg C yr^{-1} decade^{-1} or roughly decreases by 40%, indicating that the global mean trend over such a short time period is strongly influenced by the interannual variability and not necessarily part of an interdecadal trend signal [*McKinley et al.*, 2011; *Fay and McKinley*, 2013]. Nevertheless, it is intriguing to see that our SOM-FFN-based estimate shows a much larger trend in the recent decade than the model-based estimates.

The most directly comparable estimates by *Park et al.* [2010] and *Rödenbeck et al.* [2014] turn out to have relatively similar long-term mean ocean uptake, but rather different levels of interannual variability and trend. The *Park et al.* [2010] estimate, which is based on extrapolating the seasonal sea surface temperature-pCO_2 relationship to the interannual timescale, has the lowest level of variability and trend. In contrast, the flux estimate by *Rödenbeck et al.* [2014], who assimilate surface ocean pCO_2 observations with a surface mixed layer scheme has the largest level of variability. Our estimate is in-between these two extremes, although in closer agreement with those of *Rödenbeck et al.* [2014] who also used SOCAT v2, although extrapolated the observations with a completely different approach.

7. A Global Carbon Budget (1998 Through 2011)

Our observation-based estimate of the ocean sink CO_2 (without the Arctic Ocean and the river outgassing flux) permits us to construct an annual global carbon budget for the years 1998 through 2011. We hereby implicitly assume, as above, that the river-induced carbon outgassing by the ocean and the Arctic fluxes remain unchanged throughout this period.

The Global Carbon Project in their recent global carbon budget (year 2014 version 2.3) reports global carbon emissions from fossil fuel burning (Em_{ff} [*Marland et al.*, 2005; http://cdiac.ornl.gov/trends/emis/meth_reg.html]) and the atmospheric accumulation rate ($\frac{dN_{atm}}{dt}$ [*Ballantyne et al.*, 2012; Ed Dlugokencky and Pieter Tans, NOAA/ESRL, www.esrl.noaa.gov/gmd/ccgg/trends/]). With these values, we can estimate the global net land flux (F^{net}_{land}) by difference:

$$F^{net}_{land} = Em_{ff} - F_{ocean} - \frac{dN_{atm}}{dt} \quad (3)$$

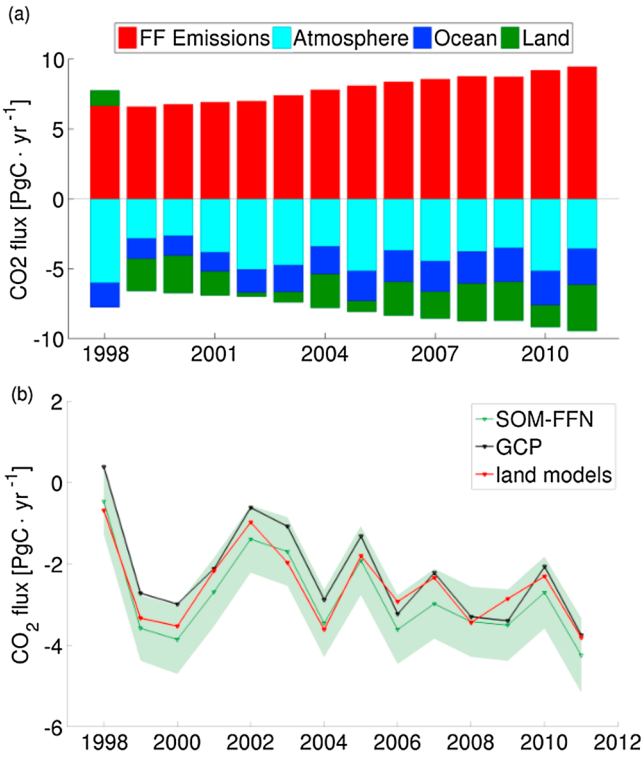

Figure 13. Annual mean global carbon budget calculated from the SOM-FFN results as (a) the sum of sources (positive) and sinks (negative) for each year from 1998 through 2011 and (b) the residual total land flux (with light green uncertainty shading) calculated from the SOM-FFN ocean flux compared to the total land flux derived from the Global Carbon Project and the mean model ensemble of the terrestrial models included in the Global Carbon budget [*Le Quéré et al.*, 2014]. Note that the land and ocean fluxes in this budget do not include the steady state carbon fluxes associated with the land-ocean aquatic continuum [*Regnier et al.*, 2013], i.e., the uptake of carbon over land to feed the carbon loss through rivers into the ocean, where it outgasses to the atmosphere.

where the net land flux does not include the CO_2 uptake component needed to compensate for the lateral carbon loss to the ocean by rivers (see *Regnier et al.* [2013] for further discussions of this land-ocean aquatic continuum). This net land flux estimate can further be used to calculate the total land CO_2 uptake flux when subtracting land use change (Em_{luc} [*Houghton*, 2003; http://cdiac.ornl.gov/trends/emis/meth_reg.html]):

$$F^{tot}_{land} = F^{net}_{land} - Em_{luc} \quad (4)$$

Figure 13a shows the annual mean carbon budget derived from this study as the sum of sources and sinks, i.e., fossil fuel emissions, atmospheric accumulation of CO_2, the carbon uptake flux by the global ocean, and the net land flux (total land flux plus land use change). Figure 13b compares our inferred total land sink estimate to the results presented by the Global Carbon Project (the implied land sink from ocean models and the mean of all land models), illustrating the strong agreement regarding the year-to-year variability, but also reflecting differences which stem from the different ocean flux estimates.

There is little doubt that the estimated SOM-FFN net land sink (F^{net}_{land}) is subject to much stronger variability than the ocean carbon sink, ranging from a net outgassing flux in the post El Niño year of 1998 of 1.12 ± 0.64 Pg C yr^{-1} to a strong sink of -3.33 ± 0.77 yr^{-1} in 2011 (Figure 13). Throughout the period 1998 through 2011, land use change describes a fairly constant source of carbon, leading to a total land flux (F^{tot}_{land}) ranging from -0.36 ± 0.87 Pg C yr^{-1} in 1998 to -4.06 ± 1.01 Pg C yr^{-1} in 2011.

Average fossil fuel emissions and land use change combined through this time period are 8.94 ± 0.64 Pg C yr^{-1}; hence, the ocean was taking up on average roughly 22% of the global emitted CO_2 from 1998 through 2011. On average, the atmospheric accumulation rate was -4.13 ± 0.17 Pg C yr^{-1}, and the resulting average total land flux was -2.82 ± 0.85 Pg C yr^{-1}, hence roughly 46% of the emitted carbon accumulated in the atmosphere, while about 32% of the emitted carbon was taken up by land from 1998 through 2011 on average.

This is in agreement with the recent carbon budget of *Le Quéré et al.* [2014], reported from 2003 through 2012, with the difference stemming from the ocean flux component, which in *Le Quéré et al.* [2014] was estimated to be -2.5 ± 0.5 Pg C yr^{-1}, largely based on model simulations that had been scaled to match the anthropogenic CO_2 uptake flux estimated by the Ocean Inversion Project of 2.2 Pg C yr^{-1} for a nominal year of 2000 [*Mikaloff Fletcher et al.*, 2006].

8. Summary and Conclusions

Here we present results regarding the mean, seasonal, and interannual variability of the air-sea CO_2 fluxes based on a recently developed neural network-based method [*Landschützer et al.*, 2013], which enables us

to estimate the sea surface pCO_2 on a monthly timescale at a high spatial resolution of 1°×1°. Thanks to its using information from similar, but data richer regions to estimate the pCO_2 in data-poor regions, our two-step neural network approach is able to produce relatively robust estimates globally, but it does not allow for a direct connection to processes. Our results show that it is now possible with the current network of surface pCO_2 observations to constrain the mean of the global ocean carbon sink within about $\pm$ 0.5 Pg C yr^{-1} and its interannual anomalies to within about $\pm$ 0.3 Pg C yr^{-1}. The analysis of our residuals show that they are in good agreement with observations from the SOCAT v2 database, and further compare well with independent data. Results for 1998 through 2011 suggest a mean contemporary uptake flux of -1.42 ± 0.53 Pg C yr^{-1}, which is in line with results from existing studies, particularly that by *Takahashi et al.* [2009]. This suggests that there is a good consensus regarding the long-term mean flux of CO_2. Our results reveal also that the global ocean CO_2 sink undergoes considerable year-to-year and intradecadal changes. From 1998 through 2011 we estimate a trend toward an increasing carbon sink of -1.00 ± 0.12 Pg C yr^{-1} $decade^{-1}$, which is, however, strongly influenced by interannual signals and therefore not yet a good estimate of a multidecadal trend. During our study period, the Pacific Ocean shows the largest interannual variability of $\pm$0.11 Pg C yr^{-1}. This signal is driven by ENSO, which we find to be the dominant mode of the global variability in the ocean carbon sink. Our results further illustrate the constraint that the surface ocean pCO_2 measurements provide to close the global carbon budget.

Acknowledgments

The research leading to these results has received funding from the European Community's Seventh Framework Programme (FP7 2007-2013) under grant agreement 238366. Further support was provided by EU grant 264879 (CARBOCHANGE) for N. Gruber, U. Schuster, and D.C.E. Bakker. Support for P. Landschützer, N. Gruber, and U. Schuster has been provided by EU grant 283080 (GEO-CARBON). We thank captains, officers, and crew of all ships on which measurements have been made that contribute to this study. The Surface Ocean CO_2 Atlas (SOCAT) is an international effort, supported by the International Ocean Carbon Coordination Project (IOCCP), the Surface Ocean Lower Atmosphere Study (SOLAS), and the Integrated Marine Biogeochemistry and Ecosystem Research (IMBER) program, to deliver a uniformly quality-controlled surface ocean CO_2 database. The many researchers and funding agencies responsible for the collection of data and quality control are thanked for their contributions to SOCAT.

References

Ashok, K., S. K. Behera, S. A. Rao, H. Weng, and T. Yamagata (2007), El Niño modoki and its possible teleconnection, *J. Geophys. Res.*, *112*, C11007, doi:10.1029/2006JC003798.

Assmann, K. M., M. Bentsen, J. Segschneider, and C. Heinze (2010), An isopycnic ocean carbon cycle model, *Geosci. Model Dev.*, *3*, 143–167, doi:10.5194/gmd-3-143-2010.

Atlas, R., R. N. Hoffman, J. Ardizzone, S. M. Leidner, J. C. Jusem, D. K. Smith, and D. Gombos (2011), A cross-calibrated multiplatform ocean surface wind velocity product for meteorological and oceanographic applications, *Bull. Am. Meteorol. Soc.*, *92*, 157–174.

Aumont, O., and L. Bopp (2006), Globalizing results from ocean in situ iron fertilization studies, *Global Biogeochem. Cycles*, *20*, GB2017, doi:10.1029/2005GB002591.

Bakker, D. C. E., et al. (2014), An update to the Surface Ocean CO_2 Atlas (SOCAT version 2), *Earth Syst. Sci. Data*, *6*(1), 69–90, doi:10.5194/essd-6-69-2014.

Ballantyne, A. P., C. B. Alden, J. B. Miller, P. P. Tans, and J. W. C. White (2012), Increase in observed net carbon dioxide uptake by land and oceans during the last 50 years, *Nature*, *488*, 70–72.

Bates, N. R. (2007), Interannual variability of the oceanic CO_2 sink in the subtropical gyre of the North Atlantic Ocean over the last 2 decades, *J. Geophys. Res.*, *112*, C09013, doi:10.1029/2006JC003759.

Bates, N. R. (2012), Multi-decadal uptake of carbon dioxide into subtropical mode water of the North Atlantic Ocean, *Biogeosciences*, *9*, 2649–2659, doi:10.5194/bg-9-2649-2012.

Battle, M., M. L. Bender, P. P. Tans, J. W. C. White, J. T. Ellis, T. Conway, and R. J. Francey (2000), Global carbon sinks and their variability inferred from atmospheric O_2 and $\delta^{13}C$, *Science*, *287*, 2467–2470, doi:10.1126/science.287.5462.2467.

Buitenhuis, E. T., R. B. Rivkin, S. Sailley, and C. Le Quéré (2010), Biogeochemical fluxes through microzooplankton, *Global Biogeochem. Cycles*, *24*, GB4015, doi:10.1029/2009GB003601.

Dickson, A. G., C. L. Sabine, and J. R. Christian (Eds.) (2007), Guide to best practices for ocean CO_2 measurements, PICES Special Publication 3, IOCCP Report No. 8, Sidney, B. C., Canada.

Doney, S., V. Fabry, R. A. Feely, and J. Kleypas (2009a), Ocean acidification: The other CO_2 problem, *Ann. Rev. Mar. Sci.*, *1*, 169–192, doi:10.1146/annurev.marine.010908.163834.

Doney, S. C., I. Lima, R. A. Feely, D. M. Glover, K. Lindsay, N. Mahowald, J. K. Moore, and R. Wanninkhof (2009b), Mechanisms governing interannual variability in upper-ocean inorganic carbon system and air-sea CO_2 fluxes: Physical climate and atmospheric dust, *Deep Sea Res., Part II*, *56*, 640–655, doi:10.1016/j.dsr2.2008.12.006.

Dore, J. E., R. Lukas, D. W. Sadler, D. M. Church, and M. J. a. Karl (2009), Physical and biogeochemical modulation of ocean acidification in the central North Pacific, *Proc. Natl. Acad. Sci. U.S.A.*, *106*, 12,235–12,240.

Fay, A. R., and G. A. McKinley (2013), Global trends in surface ocean pCO_2 from in situ data, *Global Biogeochem. Cycles*, *27*, 1–17, doi:10.1002/gbc.20051.

Fedorov, A. V., and S. G. Philander (2000), Is El Niño changing?, *Science*, *288*, 1997–2002, doi:10.1126/science.288.5473.1997.

Feely, R. A., R. Wanninkhof, C. E. Cosca, M. J. McPhaden, R. H. Byrne, F. J. Millero, F. P. Chavez, T. Clayton, D. M. Campbell, and P. P. Murphy (1994), The effect of tropical instability waves on CO_2 species distributions along the equator in the eastern equatorial Pacific during the 1992 ENSO event, *Geophys. Res. Lett.*, *21*, 277–280, doi:10.1029/93GL03212.

Feely, R. A., R. Wanninkhof, T. Takahashi, and P. Tans (1999), Influence of El Niño on the equatorial Pacific contribution to atmospheric CO_2 accumulation, *Nature*, *398*, 597–601, doi:10.1038/19273.

Feely, R. A., T. Takahashi, R. Wanninkhof, M. J. McPhaden, C. E. Cosca, S. C. Sutherland, and M.-E. Carr (2006), Decadal variability of the air-sea CO_2 fluxes in the equatorial Pacific ocean, *J. Geophys. Res.*, *111*, C08S90, doi:10.1029/2005JC003129.

Galbraith, E. D., A. Gnanadesikan, J. P. Dunne, and M. R. Hiscock (2010), Regional impacts of iron-light colimitation in a global biogeochemical model, *Biogeosciences*, *7*, 1043–1064, doi:10.5194/bg-7-1043-2010.

Garbe, C. S., et al. (2014), Transfer across the air-sea interface, in *Ocean-Atmosphere Interactions of Gases and Particles*, edited by P. S. Liss and M. T. Johnson, pp. 55–112, Springer, Berlin, Heidelberg.

GLOBALVIEW-CO2 (2011), *Cooperative Atmospheric Data Integration Project - Carbon Dioxide* [CD-ROM], NOAA ESRL, Boulder, Colo. [Available at ftp.cmdl.noaa.gov, path: ccg/co2/GLOBALVIEW, 5th January 2013.]

González-Dávila, M., J. M. Santana-Casiano, and E. F. González-Dávila (2007), Interannual variability of the upper ocean carbon cycle in the northeast Atlantic Ocean, *Geophys. Res. Lett.*, *34*, L07608, doi:10.1029/2006GL028145.

Graven, H. D., T. Guilderson, and R. Keeling (2012a), Observations of radiocarbon in CO_2 at seven global sampling sites in the Scripps flask network: Analysis of spatial gradients and seasonal cycles, *J. Geophys. Res.*, *117*, D02303, doi:10.1029/2011JD016533.

Graven, H. D., N. Gruber, R. Key, S. Khatiwala, and X. Giraud (2012b), Changing controls on oceanic radiocarbon: New insights on shallow-to-deep ocean exchange and anthropogenic CO_2 uptake, *J. Geophys. Res.*, *117*, C10005, doi:10.1029/2012JC008074.

Gruber, N., C. D. Keeling, and N. R. Bates (2002), Interannual variability in the North Atlantic Ocean carbon sink, *Science*, *298*, 2374–2378, doi:10.1126/science.1077077.

Gruber, N., et al. (2009), Oceanic sources, sinks, and transport of atmospheric CO_2, *Global Biogeochem. Cycles*, *23*, GB1005, doi:10.1029/2008GB003349.

Gurney, K., D. Baker, P. Rayner, and S. Denning (2008), Interannual variations in continental-scale net carbon exchange and sensitivity to observing networks estimated from atmospheric CO_2 inversions for the period 1980 to 2005, *Global Biogeochem. Cycles*, *22*, GB3025, doi:10.1029/2007GB003082.

Houghton, R. A. (2003), Revised estimates of the annual net flux of carbon to the atmosphere from changes in land use and land management 1850–2000, *Tellus B*, *55*, 378–390.

Ilyina, T., K. Six, J. Segschneider, E. Maier-Reimer, H. Li, and I. Nunez-Riboni (2013), The global ocean biogeochemistry model HAMOCC: Model architecture and performance as component of the MPI-Earth system model in different CMIP5 experimental realizations, *J. Adv. Model. Earth Syst.*, *5*, 287–315, doi:10.1002/jame.20017.

Ishii, M., et al. (2014), Air-sea CO_2 flux in the Pacific Ocean for the period 1990–2009, *Biogeosciences*, *11*(3), 709–734, doi:10.5194/bg-11-709-2014.

Jacobson, A. R., S. E. Mikaloff Fletcher, N. Gruber, J. Sarmiento, and M. Gloor (2007), A joint atmosphere-ocean inversion for surface fluxes of carbon dioxide: 2. Regional results, *Global Biogeochem. Cycles*, *21*, GB1020, doi:10.1029/2006GB002703.

Jones, S. D., C. Le Quéré, and C. Rödenbeck (2012), Autocorrelation characteristics of surface ocean pCO_2 and air-sea CO_2 fluxes, *Global Biogeochem. Cycles*, *26*, GB2042, doi:10.1029/2010GB004017.

Kalnay, E., et al. (1996), The NCEP/NCAR 40-year reanalysis project, *Bull. Am. Meteorol. Soc.*, *77*, 437–470.

Landschützer, P., N. Gruber, D. C. E. Bakker, U. Schuster, S. Nakaoka, M. R. Payne, T. Sasse, and J. Zeng (2013), A neural network-based estimate of the seasonal to inter-annual variability of the Atlantic Ocean carbon sink, *Biogeosciences*, *10*, 7793–7815, doi:10.5194/bg-10-7793-2013.

Le Quéré, C., J. C. Orr, P. Monfray, O. Aumont, and G. Madec (2000), Interannual variability of the oceanic sink of CO_2 from 1979 through 1997, *Global Biochem. Cycles*, *14*, 1247–1265, doi:10.1029/1999GB900049.

Le Quéré, C., et al. (2003), Two decades of ocean CO_2 sink and variability, *Tellus B*, *55*, 649–656, doi:10.1034/j.1600-0889.2003.00043.x.

Le Quéré, C., et al. (2007), Saturation of the Southern Ocean CO_2 sink due to recent climate change, *316*, 1735–1738, doi:10.1126/science.1136188.

Le Quéré, C., T. Takahashi, E. T. Buitenhuis, C. Rödenbeck, and S. C. Sutherland (2010), Impact of climate change and variability on the global oceanic sink of CO_2, *Global Biogeochem. Cycles*, *24*, GB4007, doi:10.1029/2009GB003599.

Le Quéré, C., et al. (2014), Global carbon budget 2013, *Earth Syst. Sci. Data*, *6*(1), 235–263, doi:10.5194/essd-6-235-2014.

Lenton, A., and R. J. Matear (2007), Role of the Southern Annular Mode (SAM) in Southern Ocean CO_2 uptake, *Global Biochem. Cycles*, *21*, GB2016, doi:10.1029/2006GB002714.

Lenton, A., et al. (2013), Sea-air CO_2 fluxes in the Southern Ocean for the period 1990–2009, *Biogeosciences*, *10*, 4037–4054, doi:10.5194/bg-10-4037-2013.

Lovenduski, N. S., and N. Gruber (2008), Toward a mechanistic understanding of the decadal trends in the Southern Ocean carbon sink, *Global Biochem. Cycles*, *22*, GB3016, doi:10.1029/2007GB003139.

Lovenduski, N. S., N. Gruber, S. C. Doney, and I. D. Lima (2007), Enhanced CO_2 outgassing in the Southern Ocean from a positive phase of the Southern Annular Mode, *Global Biogeochem. Cycles*, *21*, GB2026, doi:10.1029/2006GB002900.

Majkut, J. D., J. L. Sarmiento, and K. B. Rodgers (2014), A growing oceanic carbon uptake: Results from an inversion study of surface pCO_2 data, *Global Biochem. Cycles*, *28*, 335–351, doi:10.1002/2013GB004585.

Mantua, N. J., S. R. Hare, Y. Zhang, J. M. Wallace, and R. C. Francis (1997), A Pacific interdecadal climate oscillation with impacts on salmon production, *Bull. Am. Meteorol. Soc.*, *78*, 1069–1079.

Marland, G., T. A. Boden, and R. J. Andres (2005), Regional, and national fossil fuel CO_2 emissions. In trends: A compendium of data on global change, *Tech. Rep.*, Carbon Dioxide Information Analysis Center, Oak Ridge Natl. Lab., U. S. Department of Energy, Oak Ridge, Tenn.

Marshall, G. J. (2003), Trends in the Southern Annular Mode from observations and reanalyses, *J. Clim.*, *16*, 4134–4143.

Matear, R. J., and A. Lenton (2008), Impact of historical climate change on the Southern Ocean carbon cycle, *J. Clim.*, *21*, 5820–5834.

McKinley, G. A., M. J. Follows1, J. Marshall, and S.-M. Fan (2003), Interannual variability of air-sea O_2 fluxes and the determination of CO_2 sinks using atmospheric O_2/N_2, *Geophys. Res. Lett.*, *30*, 1101, doi:10.1029/2002GL016044.

McKinley, G. A., M. J. Follows, and J. Marshall (2004), Mechanisms of air-sea CO_2 flux variability in the equatorial Pacific and the North Atlantic, *Global Biogeochem. Cycles*, *18*, GB2011, doi:10.1029/2003GB002179.

McKinley, G. A., A. R. Fay, T. Takahashi, and N. Metzl (2011), Convergence of atmospheric and North Atlantic carbon dioxide trends on multidecadal timescales, *Nat. Geosci.*, *4*, 606–610, doi:10.1038/NGEO1193.

Menemenlis, D., J. Campin, P. Heimbach, C. Hill, T. Lee, A. Nguyen, M. Schodlok, and H. Zhang (2008), ECCO2: High resolution global ocean and sea ice data synthesis, *Mercator Ocean Q. Newslett.*, *31*, 13–21.

Mikaloff Fletcher, S. E., et al. (2006), Inverse estimates of anthropogenic CO_2 uptake, transport, and storage by the ocean, *Global Biogeochem. Cycles*, *20*, GB2002, doi:10.1029/2005GB002530.

Millero, F. J. (1995), Thermodynamics of the carbon dioxide system in the oceans, *Geochim. Cosmochim. Acta*, *59*, 661–677, doi:10.1016/0016-7037(94)00354-O.

Naegler, T. (2009), Reconciliation of excess ^{14}C-constrained global CO_2 piston velocity estimates, *Tellus B*, *61*, 372–384, doi:10.1111/j.1600-0889.2008.00408.x.

Nakaoka, S., M. Telszewski, Y. Nojiri, S. Yasunaka, C. Miyazaki, H. Mukai, and N. Usui (2013), Estimating temporal and spatial variation of ocean surface pCO_2 in the North Pacific using a self-organizing map neural network technique, *Biogeosciences*, *10*, 6093–6106, doi:10.5194/bg-10-6093-2013.

Nightingale, P., G. Malin, C. Law, A. Watson, P. Liss, M. Liddicoat, J. Boutin, and R. Upstill-Goddard (2000), In situ evaluation of air-sea gas exchange parameterizations using novel conservative and volatile tracers, *Global Biochem. Cycles*, *14*(1), 373–387.

Olafsson, J. (2007), Irminger sea cruise data from the 1991–2006 cruises, CARINA data set, *Tech. Rep.*, Carbon Dioxide Information Analysis Center, Oak Ridge Natl. Lab., U. S. Department of Energy, Oak Ridge, Tenn., doi:10.3334/CDIAC/otg.CARINA_IrmingerSea.

Park, G.-H., R. Wanninkhof, S. C. Doney, T. Takahashi, K. Lee, R. A. Feely, C. L. Sabine, J. Triñanes, and I. D. Lima (2010), Variability of global net sea-air CO_2 fluxes over the last three decades using empirical relationships, *Tellus B*, *62*, 352–368, doi:10.1111/j.1600-0889.2010.00498.x.

Peng, T.-H., T. Takahashi, W. S. Broecker, and J. Olafsson (1987), Seasonal variability of carbon dioxide, nutrients and oxygen in the northern North Atlantic surface water: Observations and model, *Tellus B*, *39*, 439–458.

Peylin, P., P. Bousquet, C. Le Quéré, S. Sitch, P. Friedlingstein, G. McKinley, N. Gruber, P. Rayner, and P. Ciais (2005), Multiple constraints on regional CO_2 flux variations over land and oceans, *Global Biochem. Cycles*, *19*, GB1011, doi:10.1029/2003GB002214.

Pfeil, B., et al. (2013), A uniform, quality controlled Surface Ocean CO_2 Atlas (SOCAT), *Earth Syst. Sci. Data*, *5*, 125–143, doi:10.5194/essd-5-125-2013.

Rayner, N. A., D. E. Parker, E. B. Horton, C. K. Folland, L. V. Alexander, D. P. Rowell, E. C. Kent, and A. Kaplan (2003), Global analyses of sea surface temperature, sea ice, and night marine air temperature since the late nineteenth century, *J. Geophys. Res.*, *108*(D14), 4407, doi:10.1029/2002JD002670.

Regnier, P., et al. (2013), Anthropogenic perturbation of the carbon fluxes from land to ocean, *Nat. Geosci.*, *6*(8), 597–607.

Reynolds, R. W., N. A. Rayner, T. M. Smith, D. C. Stokes, and W. Wang (2002), An improved in situ and satellite SST analysis for climate, *J. Clim.*, *15*, 1609–1625.

Rödenbeck, C., R. Keeling, D. Bakker, N. Metzl, A. Olsen, C. Sabine, and M. Heimann (2013), Global surface-ocean pCO_2 and sea-air CO_2 flux variability from an observation-driven ocean mixed-layer scheme, *Ocean Sci.*, *9*, 93–216, doi:10.5194/os-9-193-2013.

Rödenbeck, C., D. C. E. Bakker, N. Metzl, A. Olsen, C. Sabine, N. Cassar, F. Reum, R. F. Keeling, and M. Heimann (2014), Interannual sea-air CO_2 flux variability from an observation-driven ocean mixed-layer scheme, *Biogeosci. Discuss.*, *11*, 3167–3207, doi:10.5194/bgd-11-3167-2014.

Sabine, C. L., et al. (2013), Surface Ocean CO_2 Atlas (SOCAT) gridded data products, *Earth Syst. Sci. Data*, *5*, 145–153, doi:10.5194/essd-5-145-2013.

Sarma, V. V. S. S., A. Lenton, R. M. Law, N. Metzl, P. K. Patra, S. Doney, I. D. Lima, E. Dlugokencky, M. Ramonet, and V. Valsala (2013), Sea-air fluxes in the Indian Ocean between 1990 and 2009, *Biogeosciences*, *10*, 7035–7052.

Sarmiento, J., and N. Gruber (2006), *Ocean Biogeochemical Dynamics*, 503 pp., Princeton Univ. Press, Princeton, N. J.

Sarmiento, J. M., M. Gloor, N. Gruber, C. Beaulieu, A. R. Jacobson, S. E. Mikaloff Fletcher, S. Pacala, and K. Rodgers (2010), Trends and regional distributions of land and ocean carbon sinks, *Biogeosciences*, *7*, 2351–2367, doi:10.5194/bg-7-2351-2010.

Sarmiento, J. T., and E. T. Sundquist (1992), Revised budget for the uptake of anthropogenic carbon dioxide, *Nature*, *356*, 589–593.

Sasse, T. P., B. I. McNeil, and G. Abramowitz (2013), A new constraint on global air-sea CO_2 fluxes using bottle carbon data, *Geophys. Res. Lett.*, *40*, 1594–1599, doi:10.1002/grl.50342.

Schuster, U., et al. (2013), Atlantic and Arctic sea-air CO_2 fluxes, 1990–2009, *Biogeosciences*, *10*, 607–627, doi:10.5194/bg-10-607-2013.

Sutton, A., J. Mathis, C. Sabine, S. Maenner, and S. Musielewicz (2011), High-resolution ocean and atmosphere pCO_2 time-series measurements from mooring cce1_122w_33n, *Tech. Rep.*, Carbon Dioxide Information Analysis Center, Oak Ridge Natl. Lab., U. S. Department of Energy, Oak Ridge, Tenn., doi:10.3334/CDIAC/OTG.TSM_CCE1_122W_33N.

Sweeney, C., E. Gloor, A. R. Jacobson, R. M. Key, G. McKinley, J. L. Sarmiento, and R. Wanninkhof (2007), Constraining global air-sea gas exchange for CO_2 with recent bomb ^{14}C measurements, *Global Biogeochem. Cycles*, *21*, GB2015, doi:10.1029/2006GB002784.

Takahashi, T., R. Wanninkhof, R. Feely, R. Weiss, D. Chipman, N. Bates, J. Olafsson, C. Sabine, and S. Sutherland (1999), Net sea-air CO_2 flux over the global oceans: An improved estimate based on the sea-air pCO_2 difference, in *Proceedings of the Second International Symposium, CO_2 in the Oceans*, edited by Y. Nojiri, pp. 9–14, Center for Global Environmental Research, National Institute for Environmental Studies, Tsukuba, Japan.

Takahashi, T., et al. (2002), Global sea-air CO_2 flux based on climatological surface ocean pCO_2, and seasonal biological and temperature effects, *Deep Sea Res. II*, *49*, 1601–1622.

Takahashi, T., R. Weiss, R. Wanninkhof, D. Chipman, and R. Feely (2003), Global air-sea flux of CO_2: An estimate based on measurements of sea-air pCO_2 difference, *Proc. Natl. Acad. Sci.*, *94*, 8292–8299.

Takahashi, T., et al. (2009), Climatological mean and decadal change in surface ocean pCO_2, and net sea-air CO_2 flux over the global oceans, *Deep Sea Res. II*, *56*, 554–577.

Takahashi, T., S. C. Sutherland, and A. Kozyr (2013), Global ocean surface water partial pressure of CO_2 database: Measurements performed during 1957–2012 (version 2012). ornl/cdiac-160, ndp-088(v2012), *Tech. Rep.*, Carbon Dioxide Information Analysis Center, Oak Ridge Natl. Lab., U. S. Department of Energy, Oak Ridge, Tenn., doi:10.3334/CDIAC/OTG.NDP088(V2012).

Telszewski, M., et al. (2009), Estimating the monthly pCO_2 distribution in the North Atlantic using a self-organizing neural network, *Biogeosciences*, *6*, 1405–1421.

Valsala, V., and S. Maksyutov (2010), Simulation and assimilation of global ocean pCO_2 and air-sea CO_2 fluxes using ship observations of surface ocean pCO_2 in a simplified biogeochemical offline model, *Tellus B*, *62*, 821–840, doi:10.1111/j.1600-0889.2010.00495.x.

Wakita, M., S. Watanabe, A. Murata, and M. Honda (2010), Hydrographic and CO_2 data report at station K2 during the 1999–2008 cruises, *Tech. Rep.*, Carbon Dioxide Information Analysis Center, Oak Ridge Natl. Lab., U. S. Department of Energy, Oak Ridge, Tenn., doi:10.3334/CDIAC/otg.TSM_K2_1999-2008.

Wang, G., M. Dai, S. S. P. Shen, Y. Bai, and Y. Xu (2014), Quantifying uncertainty sources in the gridded data of sea surface CO_2 partial pressure, *J. Geophys. Res. Oceans*, *119*, 1–9, doi:10.1002/2013JC009577.

Wanninkhof, R. (1992), Relation between wind speed and gas exchange over the ocean, *J. Geophys. Res.*, *97*, 7373–7383.

Wanninkhof, R., and W. McGillis (1999), A cubic relationship between air-sea CO_2 exchange and wind speed, *Geophys. Res. Lett.*, *26*(13), 1889–1892.

Wanninkhof, R., W. E. Asher, D. T. Ho, C. Sweeney, and W. McGillis (2009), Advances in quantifying air-sea gas exchange and environmental forcing, *Ann. Rev. Mar. Sci.*, *1*, 213–244, doi:10.1146/annurev.marine.010908.163742.

Wanninkhof, R., et al. (2013a), Global ocean carbon uptake: Magnitude, variability and trends, *Biogeosciences*, *10*, 1983–2000, doi:10.5194/bg-10-1983-2013.

Wanninkhof, R., D. C. E. Bakker, N. Bates, A. Olsen, T. Steinhoff, and A. J. Sutton (2013b), Incorporation of alternative sensors in the SOCAT database and adjustments to dataset quality control flags, *Tech. Rep.*, Carbon Dioxide Information Analysis Center, Oak Ridge Natl. Lab., U. S. Department of Energy, Oak Ridge, Tenn., doi:10.3334/CDIAC/OTG.SOCAT_ADQCF.

Watson, A. J., et al. (2009), Tracking the variable North Atlantic sink for atmospheric CO_2, *Science*, *326*(5958), 1391–1393, doi:10.1126/science.1177394.

Wetzel, P., A. Winguth, and E. Maier-Reimer (2005), Sea-to-air CO_2 flux from 1948 to 2003: A model study, *Global Biochem. Cycles*, *19*, GB2005, doi:10.1029/2004GB002339.

Wolter, K., and M. S. Timlin (2011), El Niño/Southern Oscillation behaviour since 1871 as diagnosed in an extended multivariate ENSO index (MEI.ext), *Int. J. Climatol.*, *31*, 1074–1087.